Shear-enhanced electrical conductivity of synthetic quartz-graphite gouges: Implications for electromagnetic observations in carbonaceous shear zones

Jinyu Chen[1], J. Chen[1], Lu Yao[1], and Xi Ma[1]

[1]Institute of Geology, China Earthquake Administration

October 27, 2023

Shear-enhanced electrical conductivity of synthetic quartz-graphite gouges: Implications for electromagnetic observations in carbonaceous shear zones

Jinyu Chen[1], Jianye Chen[1], Lu Yao[1], Xi Ma[1]

[1]State Key Laboratory of Earthquake Dynamics, Institute of Geology, China Earthquake Administration, Beijing 100029, China.

Corresponding author: Jinyu Chen (jinyu@ies.ac.cn), Jianye Chen (jychen@ies.ac.cn)

Key Points:

- Experiments work shows that the presence of graphite can cause abrupt increase in electrical conductivity at limited shear displacement
- Graphite–cortex clasts develop in the strain-localized zone
- Initiated slips at carbonaceous shear zones can be detected by monitoring temporal electromagnetic anomalies

Abstract (248 words)

Graphite is considered as a material that promotes fault weakening and electrical conductivity (σ) enhancement at fault zones. We studied how shear deformation may affect the evolution of friction and electrical conductivity of synthetic quartz (Qz)-graphite (Gr) mixtures and, more importantly, whether the σ of the mixtures present visible changes at the beginning of the simulated fault slip. Long-displacement friction experiments were performed on 1.2–2.3 mm-thick gouge specimens of varied Gr volume fraction (X_{Gr} = 0–100 vol.%) under identical normal stress (2 or 5 MPa), slip rate (~1.0 mm/s), and N_2-flushing conditions. The experimental results suggested that the σ of the specimens with ≥ 4.6 vol.% X_{Gr} abruptly increased under limited shear displacement. With continued shear, the steady-state electrical conductivity (σ_{ss}) increased by more than seven orders of magnitude when X_{Gr} > 3.4 vol.%, while the steady-state frictional coefficient remained high (0.54–0.80) except for the specimens with X_G > 13.6 vol.%. The post-mortem microstructures revealed that the high σ_{ss} observed in the intermediate Gr content specimens (3.4–13.6 vol.%) is associated with an *ad-hoc* fabric (graphite–cortex clasts) present in the principal slip zone. For high Gr content, excess Gr flakes fill the pores and help develop mechanically lubricated surfaces. We propose that low Gr content (i.e., as low as 3.4 vol.%) can cause high conductivity anomalies in natural shear zones. Overall, the findings suggest that the initiation of slips within carbonaceous shear zones can be detected by identifying unusual temporal signals using electromagnetic stations.

Plain Language Summary (172 words)

Crystalline graphite (Gr) can be enriched within fault zones due to mechanical or chemical processes and is considered a material that promotes fault weakening and electrical conductivity enhancement at fault zones. Geophysical observations suggest highly conductive anomalies in the carbonaceous shear zones and low apparent resistivity anomalies prior to an earthquake. Given this, we designed a novel experimental assembly to conduct electrical conductivity measurements on Gr-bearing fault rocks along a fault-parallel direction during a progressive fault slip in the laboratory. Our results revealed notably enhanced electrical conductivity under limited shear displacement, corresponding to the beginning of the simulated fault slip. With continued shear, the steady-state electrical conductivity increases by more than seven orders of magnitude as the Gr content exceeds 3.4 vol.%, while the steady-state frictional coefficient remains high until the Gr content exceeds 13.6 vol.%. Our results demonstrate that interconnected Gr networks are one of the main mechanisms that can explain high conductivity anomalies at shear zones and facilitate the detection of initiated slips in carbonaceous shear zones using electromagnetic stations.

1. Introduction

Foliated fault rocks with anastomosing-network fabric composed of weak minerals (mostly phyllosilicate or carbonaceous materials [CMs]) are widely reported at natural fault zones (e.g., Collettini et al., 2009; Collettini et al., 2019; Kuo et al., 2022; Manatschal, 1999; Oohashi et al., 2012). As revealed by their surface outcrops, CMs are present in several shear zones, especially in deep ductile shear bands (e.g., Kedar et al., 2020; Lyu et al., 2020; Nakamura et al., 2015; Puelles et al., 2014; Rawat & Sharma, 2011). Recent studies also report that CMs are occasionally locally present in shallow brittle fault zones, such as in coseismic surface ruptures (e.g., Kouketsu et al., 2017; Oohashi et al., 2012; Togo et al., 2011) or in drilling boreholes across principal slip zones (e.g., Chen et al., 2016; Hirono et al., 2009; Kirilova et al., 2018b; Kuo et al., 2014; Zulauf et al., 1999). The fraction of CMs varies among carbonaceous fault zones. Most fault gouges contain ~1–36% CMs (Chen et al., 2017; Chen et al., 2016; Nakamura et al., 2015; Wang et al., 2014). Some contain even 2–12 wt.% of crystalline graphite (Gr), a special member of CMs (Manatschal, 1999; Oohashi et al., 2012). Due to diffusive mass transfer or fluid precipitation during faulting, CMs can progressively become enriched toward the center of fault zones (i.e., the principal slip zones) to accommodate large shear deformation (Kuo et al., 2014; Oohashi et al., 2012; Oohashi et al., 2013). Moreover, Gr-bearing shear zones show low electrical resistivity in magnetotelluric (MT) surveys, generally in the range of 0.100–0.005 S/m (e.g., Pous et al., 2004; Ritter et al., 2005; Wannamaker et al., 2002; Zhao et al., 2012).

Mechanical tests on binary (or ternary) mixtures of hard and weak minerals show that the shear strength of mixtures monotonically decreases with increasing content of weak minerals (Crawford et al., 2008; Moore & Lockner, 2011; Takahashi et al., 2007; Tembe et al., 2010). In particular, highly crystalline Gr has been characterized as a "dry" solid lubricant of fault zones because of its sheet structure held together solely by van der Waals forces (Kirilova et al., 2018a;

Moore & Lockner, 2004). Previous studies have shown that the steady-state frictional coefficient of Gr can remain at very low values (between ~0.1 and ~0.2) over a wide range of slip rates (5×10^{-4}–1.3 m/s) (Kirilova et al., 2018a; Oohashi et al., 2011; 2013). Even a small amount of Gr (~10 vol.%) in a fault gouge can mechanically smear on the principal shear plane. It makes fault rocks dramatically weaker than expected when considering Byerlee's law (0.6–0.85 in friction coefficient, Byerlee, 1978; Oohashi et al., 2013; Rutter et al., 2013).

Grain-boundary Gr films (a few ppm), with thicknesses ranging from a few to several tens of nanometers, can produce highly interconnected conductive networks. Their electrical conductivity reaches 0.005–0.010 S/m (Duba & Shankland, 1982; Frost et al., 1989; Glover & Vine, 1992; Mareschal et al., 1992). Such films may exist in the range of crustal depth (Selway, 2013). They have been considered as a potential mechanism explaining high conductivity anomalies in crustal shear zones (Chen et al., 2017; Glover & Ádám, 2008; Haak et al., 1997; Monteiro Santos et al., 2002). Moreover, apparent resistivity anomalies prior to an earthquake (typically descending by 1~7%) detected by electromagnetic stations have been considered as a precursor factor in medium- or short-term earthquake prediction (e.g., Du, 2011; Honkura et al., 2013; Lu et al., 2016; Madden et al., 1993; Zhao & Qian, 1994) despite their strong spatial anisotropy. Nover et al. (2005) showed that shearing deformation can enhance the electrical conductivity of carbon-bearing rocks by about three orders of magnitude. Glover & Ádám (2008) attributed this enhancement to the smearing effect and proposed that this effect can explain many precursory and coseismic geoelectric phenomena observed in nature (Mathez et al., 2008; Roberts et al., 1999). However, to date, there are insufficient systematic real-time observations of the mechanical and electrical characteristics of shearing carbon-bearing gouges. It leads to incomplete theoretical support for explaining the origin of high conductivity anomalies in deep shear zones and effectively obtaining the frictional slip information in shallow fault zones.

In this study, we used a rotary shear apparatus to conduct continuous electrical conductivity measurements on controlled-dry, synthetic, Gr-bearing gouges along the fault-parallel direction during progressive fault slip. The experiments were conducted at fixed velocity (~1 mm/s), normal stress (2 or 5 MPa), and under ambient temperature, N_2 atmosphere conditions. Results showed that an increasing Gr content can effectively reduce the frictional strength, while an initial very limited shear displacement causes an abrupt enhancement of the electrical conductivity. We further investigated the microstructure evolution of specimens with different Gr contents and found that the high electrical conductivity observed might be related to the development of Gr flakes on the grain boundaries. Our work gives insights into the coupling effect between frictional strength and electrical conductivity of Gr-bearing fault zones. Additionally, it offers experimental evidence for detecting initiated slips using electromagnetic approaches.

2. Materials and methods

2.1. Starting materials

The starting materials used in our experiments were commercial Gr powders (Xilong Scientific Co., Ltd., analytical grade, > 98.5% purity, Figure S1a in Supporting Information) and Quartz (Qz) particles (collected from Fengyang County, Anhui Province, China P.R., > 99.3% purity, Figure S1b in Supporting Information). The sizes of the Qz particles were determined by laser diffraction analysis (Microtrac S3500), which resulted in a median diameter of 12.2 μm and a size distribution comparable to that of natural fault gouges (Chen et al., 2017) (Figure S1c in Supporting Information). Synthetic fault gouges were prepared by mixing the Qz particles with Gr powders in contents of 0, 3, 4, 5, 6, 9, 10, 12, 15, 25, 50, and 100 wt.%. According to the particle densities (2.31 g/cm^3 for Gr and 2.66 g/cm^3 for Qz) measured by the true density analyzer (AccuPyc II 1340, errors ± 0.03%), the estimated volumetric percentages of Gr in the mixtures were 0.0, 3.4, 4.6, 5.7, 6.8, 10.2, 11.3, 13.6, 16.9, 27.7, 53.5 and 100 vol.%, respectively.

2.2 Experimental assembly adapted to friction–conductivity measurements

The experiments were conducted using the low- to high-velocity rotary shear apparatus installed at the Institute of Geology, China Earthquake Administration (IGCEA) (Figures 1a–1c). For this instrument, the variation of axial force (i.e., normal stress) could be controlled within 2–3%, the resolution of shear displacement is ~30 μm, and the accuracy of the measured shear torque is greater than 99% (Ma et al., 2014). We adapted a ring-shear setup for gouge-type friction experiments to monitor the transient electrical conductivity (real-time response of the electrical conductivity, σ) of simulated faults (Figure 1d) in their fault-parallel direction (Figure

1e). For testing the assembly, a simulated gouge layer with ~2.0 mm thickness was uniformly placed between a pair of 40 mm-long corundum hollow cylinders with an inner diameter (l_i) of 28 mm and an outer diameter (l_o) of 40 mm, respectively. In previous experiments that used the ring-shaped assembly, before our adaptation, the gouge layer was typically confined by the tightly fitted outer and inner Teflon® sleeve/cylinder to minimize gouge extrusion (e.g., Boulton et al., 2017; Hou et al., 2012; Yao et al., 2013a; Yao et al., 2013b). However, in the designed setup, to allow the electrical conductivity measurement, two titanium-alloy electrodes (a loop and a centered vertical cylinder) were embedded into the outer Teflon® sleeve and inner cylinder, respectively (Chen, 2022; Han et al., 2019). To avoid direct contact between the upper (rotary) corundum cylinder and the electrodes, the gap between them was kept at ~100 μm. We note that a small quantity of gouge was expected to extrude into the gaps during the experiments. It could presumably cause some uncertainty in the friction data. One or two lead wires led respectively from the two stainless steel screws on the two electrodes (Figure 1b). They were connected to the Keithley instruments (Tektronix Company, U.S.) used to measure the electrical resistance (R_E). In addition, a suit of plastomers fixed the three-layered outer sleeve to the lower corundum cylinder. Finally, to achieve a dry and anoxic environment, the whole assembly was enclosed by a transparent polymethylmethacrylate (PMMA) vessel. A (high purity) N_2 atmosphere was maintained inside the vessel during the experiment.

2.3 Experimental procedure and data processing

A total of 19 experiments were performed on the different Gr–Qz mixtures under constant normal stresses (P_n = 2 or 5 MPa) and room temperature conditions. The specimens were oven-dried at ≥ 75 °C for > 24 h prior to the experiments. After setting up each specimen assembly, it was first compacted at the target P_n for 2–3 h and then sheared at a constant slip rate of 0.83–1.00 mm/s under dry conditions.

During the experiments, three Keithley instruments (6514 System Electrometer, 2182A Nanovoltmeter, and 6221 DC and AC Current Source) were used to measure R_E. These instruments are commercial products. They enable fast, precise, high-sensitivity measurements of various electrical parameters and have been widely used for constraining the electrical properties of geological materials (e.g., Hou et al., 2021; Yamashita et al., 2014; Zhuang et al., 2021). As the R_E values of our simulated specimens varied by almost 14 orders of magnitude (from 100 GΩ to 1 mΩ), we used three different configurations and measurement modes depending on the R_E range. Thereby, the electrical potential (E) and direct current (I) [$R_E = E/I$, 4 wires setup] or R_E (2 wires setup) of the specimens were acquired. Details on the resistance measurement models and corresponding measurement accuracies are presented in Table 1. The R_E values were obtained by subtracting the background levels (0.0041 Ω). They contained the electrical resistance of the aluminum wires in the assembly and the Keithley instruments, which were assessed from the electrode-to-electrode measurement. The σ values were calculated by taking the inverse of the R_E values and normalizing them with the scale as follows:

$$\sigma = \frac{\ln(l_o/l_i)}{2\pi\delta R_E} \tag{1}$$

where δ is the thickness of the simulated gouge layer (mm). In some experiments, we paused the motor for ~5 min to switch the measurement mode due to technical issues or unexpected changes in σ. The consistency of the σ results between two modes demonstrates the relative accuracy of our measurements.

Besides recording electrical data, the axial load, axial displacement, torque, and upper piston rotation were also recorded at 20 Hz using a digital data recorder (KYOWA EDX-100A). The raw data were processed to obtain P_n, δ, equivalent slip velocity (v_e, m/s), equivalent shear stress (τ, MPa), and apparent friction coefficient ($\mu=\tau/\sigma_n$) *vs* shear displacement (D) (Ma et al., 2014). The μ value was calculated after correcting the Teflon® friction (Hou et al., 2012). As R_E was also recorded at 20 Hz using the Keithley instruments, we carefully synchronized the two recording systems by matching the feature points of R_E.

For quantitative comparison between the two quantities, we determined several critical parameters from the μ and σ *vs* D curves (Table 2, Figures 2–3). For instance, μ_{ss} and σ_{ss} are the nominal (quasi-) steady-state frictional coefficient and electrical conductivity achieved at long displacement. They were obtained from the arithmetically average value of μ in steady state and the logarithmically average value of σ in steady state, respectively. $D_{\mu ss}$ and $D_{\sigma ss}$ are the corresponding characteristic displacements. Moreover, we defined $D_{\sigma ch}$ as the critical slip displacement for abrupt electrical conductivity enhancement (i.e., σ-jump phenomenon). Namely, the σ curve, for the first time, shows an increase by more than one order of magnitude from the low initial level (σ_0 < 0.01 S/m), or more than 1.5 times from a high initial level (σ_0 > 0.01 S/m). For details on the data processing and determination of the critical parameters, we refer to Text S1 and Figure S2 in Supporting Information.

After the experiments, a scanning electron microscope (SEM, Zeiss Sigma-0380) was used to examine the microstructural developments as a function of the Gr content (Figure 1e). The scanning electron microscope was operated at an acceleration voltage of 15 kV in both the backscatter electron (BSE) and secondary electron (SE) modes. Microstructural images were taken from the corresponding Au-coated thin sections.

3. Results

The experimental data obtained from the 19 experiments (with the synthetic fault gouges) are presented in Table 2. As described in section 2.3, two series of data were obtained using our rotary-shear friction apparatus adapted for conducting transient electrical conductivity measurements.

3.1 General mechanical and electrical behaviors

Figure 2 presents the mechanical (panels a–b) and electrical (panels c–d) behaviors of the Gr–Qz mixture specimens. They were sheared at a normal stress of 2 MPa as a function of slip displacement in both logarithmic (panels a and c) and linear (panels b and d) scales. With low to intermediate Gr contents (< 25 wt.%), the specimens exhibited peak friction coefficients of 0.49–0.67 at less than 0.17 m slip displacement (Figure 2a). Then, it was followed by slip strengthening to ~1 m and overall high friction levels (0.54–0.80) in the end (Figure 2b). With high Gr contents (25–50 wt.%), the peak friction reached 0.40–0.51 at a displacement of ~1 mm, followed by dramatic slip weakening with steady-state friction coefficients of 0.10–0.19. At a high normal stress of 5 MPa, similar frictional behaviors were evident for both low and high Gr contents (Figure 3a).

The specimens showed large variations in electrical conductivity of up to 14 orders of magnitude (i.e., from 10^{-11} to 10^{3} S/m), depending on the Gr content and shear displacement. (1)

For Gr content < 4 wt.%, σ decreased slightly with initial shear displacement. (2) For Gr content of 4–10 wt.%, the specimens showed intermediate σ_{ss} values in the range of 10^{-3}–0.3 S/m. Interestingly, σ increased remarkably with the slip progression after $D_{\sigma ch}$ by more than six orders of magnitude. (3) Specimens with Gr contents > 12 wt.% showed slight increases (a few times) in σ with slip. The σ maintained high values (> 0.1 S/m) throughout the experiments.

3.2 Comparison of characteristic displacements

The results of the σ–D and μ–D data by Gr content are presented in Figure 4. To reveal the possible links between σ and μ, we highlight the σ and μ evolution at displacements between $D_{\sigma ch}$ and $D_{\sigma ss}$, during which σ increased significantly.

The initial nearly-linear portions of the μ–D curves reflect the elastic shear loading processes. Because the displacements in all μ–D and σ–D plots are precisely the load point displacements that embody the shear deformation of the entire testing system. The displacements at which the μ–D curves deviate from straight lines are the starting points of the shear deformation in the gouge layers (see the circle symbols in Figures 4d–4f, hereafter referred to as D_0). Thus, the difference between D_0 and $D_{\sigma ch}$ represents the shear displacement required to initiate the generation of a continuous electrically conductive layer associated with the shear deformation of the Gr–Qz mixtures. Since the D_0 values of all specimens are small and not very different from one another (typically ~0.15–0.28 mm), we plotted $D_{\sigma ch}$ against the Gr content in Figure 4g and Figure 4h, while $D_{\mu ss}$ and $D_{\sigma ss}$ were plotted for comparison. As the Gr content increased, the $D_{\sigma ch}$ value decreased from 0.5 m, via 4 mm, to 0.2 mm; similarly, $D_{\sigma ss}$ decreased from 1.2 m, via 100 mm, to 3.0 mm. In contrast, $D_{\mu ss}$ seemed to be independent of the Gr content, thereby remaining at high values (mostly between 0.3 and 0.6 m). Therefore, $D_{\sigma ch}$ and $D_{\sigma ss}$ were significantly lower than $D_{\mu ss}$ at Gr content higher than ~9 wt.%. Consequently, for the mixtures with 4–12 wt.% Gr, the critical slip displacement for the σ jump ($D_{\sigma ch}$) was limited (as low as 0.2 mm) and smaller than the displacement for reaching the frictional steady state ($D_{\mu ss}$) (see the start of the bold curves in Figures 4d–4e). The σ jump occurred before the peak friction, even in the case of mixtures with high Gr content (15–50 wt.%) (see the start of the bold curves in Figure 4f).

3.3 Microstructural evolution in steady state

As revealed by the BSE images of the epoxied post-mortem specimens, with increasing Gr content (0, 3, 9, and 25 wt.%), the specimens became increasingly cohesive after the experiment. The pure Qz gouge was the most fragile, showing a loose structure, whereas the high Gr content gouge layer could be recovered as an entire piece (Figure 5). A slickenside surface ornamenting the discrete shear surface of a high-Gr portion specimen was observed after the experiment (attached picture on top of Figure 5d), while a dark surface appeared on the surface of a low-Gr portion specimen (attached picture on top of Figure 5c).

The pure Qz gouge did not show a discernable strain localization zone (SLZ). However, discrete inclined openings were visible over the entire thickness, mostly along the Riedel shear (R shear, Logan et al., 1992), oriented at a low angle of 10°–30° to the shear direction (Figure 5a). In contrast, remarkable shear bands were developed at the upper rotary boundaries in the other mixture specimens, especially those with low Gr contents (3 and 9 wt.%, Figures 5b and 5c). In these two specimens, the angular fractured Qz particles of the lowest layer had relatively large grain sizes, similar to that of the pure Qz gouge (Layer III). The localized band was further divided into two layers (see the yellow dotted lines for the boundaries, Figures 5b and 5c). Generally, the middle layer was homogeneous, and its average grain size (~5 μm) was lower than that of the least deformed layer. The uppermost layer had the finest grain size, mostly lower than ~1 μm. In a certain portion of this layer, agglomerated clumps of extremely fine Qz particles developed, characterized by thicknesses of ~10 μm and lengths varying from a few tens to a few hundreds of micrometers. Locally, they were cut by the R shear offset, manifested as discrete stripes parallel to the shear direction (Figures 5b and 5e). Such discrete clumps were interpreted as the migration of the microslip zone during extreme shearing deformation, in accordance with previous reports (Yao et al., 2013a; Yao et al., 2013b). The enlarged pictures indicate that these clumps were characterized by homogenous Qz grain size distribution and had extremely low porosity (< 5%, estimated based on image analysis, Figure 5e), while the remainder of the upper layer had a broader grain size distribution (varying from 0.1 to 1.0 μm) and relatively high porosity (20–30%, Figure 5f). Gr flakes, with widths of up to several tens of nanometers, filled the space between the Qz particles to form anastomosing networks (Figure 5f). Consequently, the microslip zone was developed from the middle layer and grew toward the upper boundary as the slip proceeded, as revealed by the comparison of the microstructures between Layers I and III. The microstructure of the high Gr specimen (25 wt.%) showed extremely localized deformation, and the shining surface on the specimen formed a 10–20 μm layer (Figure 5d). The enlarged picture shows deflected Gr flakes that formed anastomosing networks around broken Qz particles.

The Gr and the epoxy resin were difficult to distinguish at the submicron scale based on SEM images. Thus, we directly observed the unepoxied specimens of 12 wt.% Gr-bearing recovery specimen (LHV2429) under a top view perspective (Figure 6a). The upper boundary showed a relatively smoothed surface, consisting of fine Qz particles of ~1–2 μm with sub-angular shape and submicron Gr flakes. It was consistent with Layer I identified in the thin section (Figure 6b). The enlarged image shows that the individual Qz particles were pasted on the surface by a large amount of small Gr flakes (Figure 6c). In contrast, the broken surface beneath the upper surface (see its position in Figure 6a) had relatively large particles (~10 μm) (Figure 6d). The individual Qz particles were mostly angular without visible foliation, while Gr appeared as isolated grains, suggesting relatively small deformation (Figure 6e). Note that numerous small particles were seen to be attached to the surfaces of Qz particles, but most were Qz debris (Figure 6f). All these features were similar to those observed in Layer III of specimens with intermediate Gr wt.% (i.e., 3 and 9 wt.%).

4. Discussion

4.1 Mechanical and electrical behaviors of graphite-bearing faults

4.1.1 Steady-state friction and conductivity relations of varying X_{Gr} specimens

To facilitate the comparison with previous works, the Gr fractions of all specimens were transformed from weight percentages to volume percentages (X_{Gr}). Figure 7 shows μ_{ss} and σ_{ss} plotted against X_{Gr} for all specimens.

The μ_{ss}–X_{Gr} data determined a threshold value (~13.6 vol.%), i.e., the X_{Gr} at which the frictional strength starts to decrease. A systematic increase of X_{Gr} from ~13.6 to 30 vol.% led to a nonlinear μ_{ss} decrease from 0.72 to 0.14. Thereafter, when X_{Gr} changed from 30 to 100 vol.%, μ_{ss}

gently approached μ_{Gr} (~0.1). Oohashi et al. (2013) conducted frictional experiments on Gr–Qz mixtures under similar conditions (σ_n = ~2 MPa, dry, v_e = 0.2–56.0 mm/s, X_{Gr} = 0–100 vol.%) and observed similar weakening trends as X_{Gr} increased (although they did not measure σ_{ss}). Following Oohashi et al. (2013), the relationship between μ_{ss}–X_{Gr}, in this study, can be described by

$$\mu_{ss}\ (X_{Gr}) = \frac{\mu_{Qz}\text{-}\mu_{Gr}}{1+(X_{Gr}/X_{cw})^{S}} + \mu_{Gr}, \tag{2}$$

where μ_{Qz} and μ_{Gr} are the frictional coefficients of pure Qz and pure Gr, respectively. The μ_{Qz} (0.73) was taken as the mean value of μ_{ss} for the low-X_{Gr} specimens (< 13.6 vol.%), and μ_{Gr} was taken as 0.10 based on the μ_{ss} values of pure Gr flakes. X_{cw} is the critical X_{Gr}, at which friction reduces to the averages of μ_{Qz} and μ_{Gr}. The power exponent S indicates the slope of the weakening with increasing X_{Gr}. The fitted parameters are presented in Table 3, and the correlation coefficient (R^2) is 0.94.

The σ_{ss} results show a significant sharp increase when X_{Gr} exceeds 3.4 vol.% (i.e., by more than 7 orders of magnitude from 3.4 to 4.6 vol.%, Figure 7) and the σ_{ss} of pure Gr flakes (10^3 S/m) is much greater than that of pure Qz particles (10^{-11} S/m). The enhancement of σ caused by Gr has been observed in high pressure and/or high temperature experiments under static conditions (Chen et al., 2017; Wang et al., 2013). In particular, Chen et al. (2017) explored the electrical conductivity of similar Qz–Gr mixtures under non-sheared deformation and a wide range of stress from 0.1 to 300.0 MPa. Following a previous study, percolation theory, i.e., a model describing well the current transport properties through porous mediums (Stauffer & Aharony, 2003), can explain the trend of the σ_{ss}–X_{Gr} curve via the following equation (Gueguen & Dienes, 1989):

$$\sigma_{ss}\ (X_{Gr}) = \sigma_{Qz} + \left(\sigma_{Gr}\text{-}\sigma_{Qz}\right)\left[\frac{\alpha(X_{Gr}\text{-}X_c)}{1\text{-}\alpha X_c}\right]^{r}, \qquad (X_{Gr} \geq 3.4\%) \tag{3}$$

where σ_{Qz} and σ_{Gr} are the electrical conductivities of the relatively insulated matrix (Qz) and conductive inclusion (Gr), α is the geometric factor of the conductor (Gr), and r is a nondimensional parameter. X_c is the threshold value of X_{Gr}. It represents the critical volume fraction of the conductor (Gr flakes in this study) for forming interconnected networks in the specimens and depends on the geometry of the Gr flakes (Stauffer & Aharony, 2003). We note that this study focuses on the effect of shear, especially the experimental data of low to intermediate X_{Gr} specimens (< 20 vol.%). Therefore, data of high-X_{Gr} specimens (> 20 vol.%) are more scarce and cannot provide a better fitting for the power law growth. The fitted parameters of Equation 3 are presented in Table 4, and the correlation coefficient (R^2) is 0.98. Other fitting details of the μ_{ss}–X_{Gr} and σ_{ss}–X_{Gr} relationships can be found in Text S2.

4.1.2 Representative microstructure interpretation

The critical X_{Gr} value for a μ_{ss} decrease (~13.6 vol.%) was greater than that for a σ_{ss} increase (3.4 vol.%) (as shown by the comparison between the μ_{ss}–X_{Gr} and σ_{ss}–X_{Gr} curves in Figure 7). It may be caused by the specific microstructural variations of the Qz–Gr mixtures. Consequently, we divided this system into three regimes bounded by 3.4 and ~13.6 vol.% X_{Gr}, respectively. For carbon-bearing rocks, the efficient electrical conductivity enhancement is mainly derived from the microstructure of interconnected grain-boundary CMs (Duba & Shankland, 1982; Frost et al., 1989; Mareschal et al., 1992). Associated with the SEM images in Figures 5 and 6, we propose four classes of microstructures dependent on X_{Gr} (T1–T4, see the schematic diagrams beneath the coordinate system of Figure 7) as follows:

(a) Pure Qz gouge (X_{Gr} = 0). It exhibited insulating (~10^{-11} S/m) and high-shear strength properties ($\mu_{ss} \approx 0.73$). A fault slip formed at the contact between Qz particles, and R-shear surfaces developed throughout the entire mixture.

(b) Low X_{Gr} regime (0% < $X_{Gr} \leq 3.4\%$). Similar to pure Qz gouge, it presented low electrical conduction (~10^{-10} S/m) and high-level frictional strength (0.79–0.85). Three layers with different Qz grain sizes (Layers I–III) developed, and similar results have been reported in natural gouges (Hou et al., 2012; Wang et al., 2014). The non-foliated layer (Layer III), in the bottom, comprised isolated angular Qz particles mixed with Gr flakes. The upper ~400 μm SLZ consisted of an ~200 μm Layer I, and an ~200 μm Layer II was produced near the side of the specimen–cylinder boundary (grey layers in Figure 7). Moreover, low σ_{ss} of the mixtures in this regime suggests the conductive Gr flakes cannot interconnect in this microstructure.

(c) Intermediate X_{Gr} regime (3.4% < $X_{Gr} \lessapprox 13.6\%$). It was characterized by σ_{ss} enhancement with increasing X_{Gr} (10^{-3} S/m < σ_{ss} < 4 S/m). It also presented a three-layered microstructure (Layers I–III) that differed from that of the low X_{Gr} regime. The Gr flakes were more frequent in the pore spaces supported by the Qz framework with increasing X_{Gr}. Unimpregnated microstructures of the slip surfaces in this regime showed a large number of tiny Gr flakes (~10 nm) pasted on the surface of Qz particles (Figures 6b and 6c). Thus, we propose that the SLZ of Qz–Gr mixtures developed the fabric of graphite–cortex clasts (GCCs), i.e., comminuted subangular Qz clasts (< 1 μm) were surrounded by a cortex of concentric Gr layers (~10 nm), which were composed of ultrafine pulverized Gr flakes (see the schematic cartoon extended from the T3 texture). In contrast, Gr flakes in this regime could not be enriched to form lubricated slip surfaces due to limited Gr fraction, and, therefore, the friction remained high (μ_{ss} = 0.54–0.84). Moreover, GCCs may also exist in the low X_{Gr} regime, but due to the low X_{Gr}, they may not be electrically connected.

(d) High X_{Gr} regime (13.6% $\lesssim X_{\mathrm{Gr}} <$ 100%). It exhibited high σ_{ss} values (> 1 S/m) and low μ_{ss} values (mostly < 0.2). In particular, specimens in this regime had an initially conductive structure ($D_{\sigma\mathrm{ch}}$ < 0.2 mm). Frictional weakening occurred during the experiment, and the required slip distances were uniform ($D_{\mu\mathrm{ss}}$ = 0.2–0.3 m, Figures 4g–4h). When the X_{Gr} was enhanced, the frictional level approached a pure Gr powder ($\mu \approx 0.1$). In this case, the specimen usually presented a narrow boundary shear band (Figure 5d) instead of a dispersive shear zone (*cf*. low X_{Gr} regimes). The single shear zone (or shining surface) with an ~20 μm thickness was similar to that of the abandoned shear surface (Qz clumps in Figure 5e).

4.1.3 Mechanisms responsible for electrical conduction and slip weakening

As addressed earlier, the σ of pure quartz and Gr–Qz mixtures with $X_{\mathrm{Gr}} \leq 3.4\%$ decreased with initial shear displacement by several orders of magnitude. We interpreted that the initial current flow was mainly through the grain contacts of large grains that developed under initial static compaction, and that the transient decrease of electrical conductivity was due to the destruction of large contacting asperities by initiating slip. A similar process has been proposed by Yamashita et al. (2014) to explain the changes in electrical conductivity of gabbro specimens sheared at subseismic velocities.

For the Gr–Qz mixtures in the intermediate X_{Gr} regime (3.4% < $X_{\mathrm{Gr}} \lesssim$ 13.6%), σ showed unstable fluctuations and eventually increased by more than six orders of magnitude during progressive slip from $D_{\sigma \mathrm{ch}}$ to $D_{\sigma \mathrm{ss}}$. In the steady state, they exhibited highly frictional strength (after $D_{\mu \mathrm{ss}}$) and electrical conduction (after $D_{\sigma \mathrm{ss}}$). Meanwhile, the SEM images showed a three-layered microstructure. We interpret that the conductive pathways mainly occurred in Layer I in the form of GCC fabric for the following reasons:

Layer III was almost undeformed and resembled an original preslip zone of the mixture. The fractures in the Qz particles may result from the axial compaction derived from the normal stress on the specimen. During the progressive slip, the original Qz particles were comminuted to micron- and even submicron-sized clasts, while subsequently producing an ~200 μm intensively foliated layer (Layer I) and an ~200 μm weakly foliated layer (Layer II), respectively. Compared with Layer I, Layer II exhibited a relatively larger Qz clast size and weak strain localization lying on the transitional phase between Layers I and III. Therefore, from the bottom to the top of the bulk gouge, the shear strain gradually increased, and the original Qz particles experienced a series of processes. They were axial compression, fragmentation, attrition, comminution, shear-induced clumping, and finally, attracting the ground Gr flakes to generate the GCC fabric in the SLZ. Several Qz clumps consisting of aggregated ultrafine Qz clasts with a thickness of ~10 μm were abandoned in Layer I. The pore-filled Gr flakes between the Qz particles also underwent microstructural evolution from disconnection to interconnection. The instability of σ from σ_{ch} to σ_{ss} corresponds to this process of microstructural transformation.

Our proposed GCC fabric is an unusual spherical aggregate. To our knowledge, this microstructure has not been published in other studies, including those of unsheared Gr–Qz mixtures (Chen et al., 2017) and sheared Gr–Qz mixtures at various slip rates (Oohashi et al., 2013). Its overall appearance resembles those of clay–clast aggregate or clast–cortex aggregate (CCA) fabrics. They were reported in previous investigations of shallow-depth seismogenic faults in the field or in rotary-shear experiments in laboratory (Boullier et al., 2009; Han & Hirose, 2012; Kim et al., 2022; Rempe et al., 2014; Sawai et al., 2012; Ujiie & Tsutsumi, 2010). We hypothesize that the formation process of the high friction–conduction GCC fabric is similar to that of the CCA formation model proposed by Boutareaud et al. (2010), i.e., electrostatically charged Qz particles by fractoemission and triboelectric effect attract Gr flakes to the "negative" Qz surface (Huang, 2002; Yoshida et al., 1997). Moreover, our results demonstrated that the GCC fabric was developed in samples with relatively low Gr contacts and required a relatively large shear displacement under room-dry conditions. These conditions are also similar to the CCA formation conditions suggested by Han & Hirose (2012); Kim et al. (2022); Rempe et al. (2014).

The Gr–Qz mixtures in the high X_{Gr} regime (13.6% $\lessapprox X_{Gr} < 100\%$) showed high σ values before shear deformation (> 0.3 S/m), suggesting that the Gr flakes were texturally interconnected upon initial compaction. With continued shear, σ further increased to even higher values (> 1 S/m), which can be attributed to the formation of the shear band. As reflected by the microstructure, the reduced porosity of the SLZ caused an apparent enrichment of Gr flakes and σ enhancement (Figure 5d). It was supported by the previous compaction experiments that elevating the static stress could cause reduced porosity and, thus, the increase in electrical conductivity (Chen et al., 2017). Meanwhile, specimens in this high X_{Gr} regime were expected to readily weaken when subjected to shear deformation (Oohashi et al., 2013). We infer this is because of the apparent enrichment of Gr flakes due to porosity reduction and the development of slip-lubricated surfaces (Figure 5d). Interestingly, the thicknesses of the slip surfaces (10–20 μm) were comparable to that of the Qz clumps developed in the intermediate X_{Gr} samples (see Figure 5e *vs.* Figure 5d). As indicated earlier, the latter were abandoned microslip zones during progressive slip, reflecting the migration of localized deformation. We infer that the single slip surface seen in the high X_{Gr} regime derived from a microslip zone developed at the earlier stage of shearing, whose resistance to shear is expected to be lower than that of the bulk layer. In all, these results suggest a strong interplay between the mineralogy, structure, and mechanical behavior of a fault.

Finally, we have used the percolation model (Equation 2) to fit the relationship between σ_{ss}–X_{Gr} of the Gr–Qz mixtures with > 3.4% X_{Gr}. The applications of the percolation theory concerning the electrical current transport properties assume that the conductor is randomly located in a stable and isotropic structure (Stauffer & Aharony, 2003). Although we applied the percolation model to describe the conductive transport properties of a sheared fault gouge, the corresponding microstructure is assumed to have reached a similar quasi-steady state, reflecting an average structure of millions of particles. Admittedly, the proposed conductive textures in the intermediate to high X_{Gr} regimes in Figure 7 are anisotropic. However, the theory model can well express the relationship between σ_{ss}–X_{Gr} under shear deformation in this study. It suggests that the percolation model could have a much wider application. Nevertheless, it still requires further adaption of the percolation model to incorporate the anisotropic transport structure.

One possible development would involve the dimensions in which the conductive material (i.e., Gr) is distributed. Nominally, one could consider that the GCCs (graphite–cortex clasts) fabric is a two-dimensional (2D) structure, i.e., the Qz particles in the shear active zone are fully covered by Gr flakes (the schematic cartoon in Figure 7). However, as suggested by a simple calculation assuming Gr flakes of varied thicknesses (10–50 nm), obtaining such a structure requires a Gr content of at least 5.7 vol.%, higher than the threshold value of 3.4 vol.% obtained in the present experiments. At this point, an electrically conductive structure in one dimension (1D), i.e., the Gr flakes are attached end-to-end on the Qz surface to reach the electrodes, can help settle the discrepancy. The real GCC fabric in the samples might fall between 1D and 2D. Moreover, this does not conflict with the observation that much higher Gr contents (>13.6 vol%) are required to cause significant frictional weakening at otherwise the same conditions (Figure 7). This is because the frictional resistance of a shearing gouge is collectively determined by all the grain contacts within the active shear zone, such that the weakening would be more favorable when the Gr flakes somehow form a 2-D structure, requiring a higher Gr content. Nonetheless, at present, it is difficult to justify the aforementioned models. A combination of numerical simulations based on more sophisticated microstructure characteristics and updated percolation models is warranted in the future.

4.1.4 Implications for high conductivity anomalies

The high conductivity anomalies in the fault zones observed by MT surveys are generally limited within the range of 0.100–0.005 S/m (e.g., Pous et al., 2004; Ritter et al., 2005; Wannamaker et al., 2002; Zhao et al., 2012). As illustrated in Figure 8, our data suggest that the Qz–Gr mixtures containing 5.4–8.1 vol.% Gr explain such observations (yellow stars in Figure 8). However, this range is higher than those reported at fault zones by geological survey results (Manatschal, 1999; Oohashi et al., 2012).

Therefore, we subjected both the initial σ_0 values and the fitted σ_{ss}–X_{Gr} curve of our study and those of previous experiments under higher static pressure conditions (Chen et al., 2017) for further discussion. The σ_0 values showed similar enhancement with increasing X_{Gr} to σ_{ss} values (from ~10^{-10} S/m to ~10^3 S/m). Under static compaction, the higher the normal stress, the lower the threshold value (X_c, 6.0% under up to 300 MPa *vs.* 11.3% under 2 MPa), while the sheared specimen has the lowest X_c value (3.4%). Therefore, we posit two enhancement factors of X_c (threshold value) and electrical conduction, i.e., shear deformation (a red shadow in Figure 8) and static compaction (a blue shadow in Figure 8). Meanwhile, deep Gr flakes can remain stable up to crustal depth (Selway, 2013). Therefore, assuming high pressure and temperature conditions, which are common in fault conditions, high σ values can be readily achieved in natural faults when X_{Gr} reaches 3.4%, given an extremely high growth rate across the critical value (upward pathway labeled by red dashed arrow in Figure 8).

The conductive properties of the upper crust can be affected by many electrical conduction factors, such as pressure, temperature, graphite (Frost et al., 1989; Nover et al., 1998), saline fluid (Guo & Keppler, 2019; Sinmyo & Keppler, 2017), sulfide (Watson et al., 2010), or partial melting (Chen et al., 2018). Furthermore, the coexistence of interconnected melt/fluids and Gr veins also seem to provide the best explanation in several low resistive fault zone derived from MT profiles (Wannamaker et al., 2002; Yu et al., 2020; Zhao et al., 2012) because the interconnected saline fluid improves the Gr-vein conduction (depositing hydrothermal Gr or promoting conductivity) (Kirilova et al., 2018b; Oohashi et al., 2012). To disentangle the effect of these mechanisms, we need to apply the control variable method, i.e., separately study these factors one by one to clarify their effects and finally summarize them and bring them together for comparison. Our work currently focuses only on the effect of Gr-bearing conductive networks on high conductivity anomalies at fault zones. Further experimental investigations at high temperatures and high pressure are necessary to constrain the mechanical and electrical conduction mechanisms of high conductivity brittle-to-ductile shear zones.

4.2 Electrical conductivity variations at initiation of frictional slip

4.2.1 Electrical conductivity jump as a potential indicator for fault slip

The results of our mechanical–electrical experiments at the millimeter scale show that the σ-jump phenomenon of Qz–Gr mixtures with > 4.6 vol.% Gr (> 4 wt.% Gr) occurred before steady-state frictional slip, and even before the peak friction (see Figures 4a–4c *vs.* Figures 4d–4f, and the inset of Figure 9). This suggests that this jump can appear before steady-state fault slip, i.e., initiated frictional slip that may generate potential electromagnetic anomaly signals (the red area in Figure 9). In the following, we apply this phenomenon to natural Gr-enriched fault zones.

According to the classic earthquake nucleation theory, quasi-static or pre-slip occurs in the local area of a fault (i.e., the nucleation zone) before an earthquake (e.g., Dieterich, 1992; Rubin & Ampuero, 2005). With the expansion of the slip region, the fault appears to have irreversible dynamic expansion as it reaches the critical nucleation scale. Therefore, based on the above experimental observations, it is possible to detect an initiated slip of the fault by monitoring the change in the σ at the nucleation zone of the fault (see the abnormal electrical signals detected by the electrical resistivity stations in Figure 9). Besides the pre-slip, continuous or periodic creep (slow slip) of faults can also cause variations in electrical conductivity values. However, we cannot determine the cumulative slip displacement of the fault zone by electromagnetic data monitoring. If the slip has accumulated too large, that will lead to the development of a more mature shear zone structure (similar to the late stage in our experiment). The abrupt change in the electrical conductivity will hardly be observed. Therefore, thus far, for actual applications, our experimental results may not provide evidence for distinguishing fault creeps.

4.2.2 Limitations and future development

Although this study is the first attempt to constrain the electrical response of carbon-bearing fault gouges under dynamic friction conditions, our conclusions have some limitations.

Firstly, the σ measurements used a single-frequency direct current method. However, the observed data of seismic georesistivity stations in the field cover a wide frequency range, which can reflect the electrical structure over various depth ranges (see the electrical current pathways at different depths in Figure 9). Although we sacrificed the accuracy of the electrical measurements, the transient electrical conductivity and the corresponding characteristic displacements of sheared fault gouge can be obtained in this study. In fact, our experimental data obtained based on the DC single-frequency method are close to those measured by the AC impedance spectroscopy on the same sheared Gr–Qz mixtures at the same conditions (Han et al., 2019). We believe that the precision of the experimental data meets the requirements of this study.

Secondly, only the specimens with > 17 vol.% Gr (or > 15 wt.% Gr) under our experimental conditions (i.e., low normal stress, room temperature, and dry conditions) exhibited the σ-jump phenomenon prior to the peak friction (Figure 4f). Fluid is widely present in nature fault zones and plays important roles in various aspects (Hickman et al., 1995). Previous studies also proposed that electrical anomalies in the brittle shallow fault zone are caused by pore fluid within rock fractures (Du, 2011; Park et al., 1993; Zhao & Qian, 1994). Against this background, the electromagnetic anomaly signals due to Gr interconnection revealed in this study may be limited to anhydrous fault environments, such as deep cataclasites with low porosities (bold blue dashed line across the preslip zone in Figure 9). Temperature and pressure conditions may also affect the results. Our previous experiments under static conditions revealed that elevated pressure can facilitate the grain-boundary Gr conduction and significantly reduce the threshold value (i.e., from 11.3 to 6.0 vol.% as pressure increases to 300 MPa, Figure 8). Taking this effect into account, the electromagnetic anomaly is expected to be generated under short shear displacement and/or lower threshold value. As indicated earlier, a natural Gr-bearing fault may have Gr content up to 12 wt.% (Manatschal, 1999; Oohashi et al., 2012). At elevated temperatures, plastic deformation mechanisms come to play an increasing role, and at some point, the silicate minerals begin to exhibit semiconductor behavior (e.g., >200–300 °C, Selway, 2013). All these processes can enhance the conductivity and affect the threshold values (Wang et al., 2013). To investigate these effects, systematical experiments using high-temperature and high-pressure deformation apparatuses such as the Paterson rig are planned in the future.

5 Conclusions

We designed a rotary-shear setup to monitor the transient electrical response of synthetic dry quartz (Qz)–graphite (Gr) mixtures in the shear-parallel direction during progressive slip. Long-displacement friction experiments (0.9–4.2 m) were performed at fixed normal stresses, slip rate, and N_2-flushing atmosphere.

(1) Graphite volume fraction (X_{Gr}) and slip displacement had important effects on the frictional coefficient (μ) and electrical conductivity (σ) of the mixture. The steady-state frictional coefficient (μ_{ss}) of the mixtures with low X_G (< 13.6 vol.%) maintained high levels of frictional strength (μ = 0.54–0.80), while the mixtures with high X_G (> 13.6 vol.%) showed remarkable slip

weakening behavior where the μ_{ss} decreased with the increase of X_{Gr}. The σ of the mixtures with $\geq$ 4.6 vol.% X_{Gr} abruptly increased (σ jump) with limited shear displacement; some σ jumps occurred even before the peak friction (as low as 0.2 mm). With continued shear, the steady-state electrical conductivity (σ_{ss}) increased by more than seven orders of magnitude when X_{Gr} > 3.4 vol.%. The post-mortem microstructures revealed that the high σ_{ss} observed in the intermediate Gr content specimens (3.4–13.6 vol.%) was associated with an *ad-hoc* fabric (graphite-cortex clasts, GCCs) present in the principal slip zone. Excess Gr flakes can fill the pores and help develop Gr-coated mechanically lubricated surfaces.

(2) The percolation model can capture the relationship between the σ_{ss} and X_{Gr} of the Qz–Gr mixture. However, the percolation theory required adaption in the future to incorporate the anisotropic transport structure more accurately. Compared with the observations of magnetotelluric (MT) surveys, our experimental results revealed that dry sheared fault rocks containing 5.4–8.1 vol.% Gr may be responsible for the highly conductive anomalies at shear zones. Furthermore, considering the effect of high normal stress from our previous study (Chen et al., 2017), the high electrical conductivity (σ) in the natural fault may also be achieved when the X_{Gr} is as low as 3.4 vol.%.

(3) The observed σ-jump phenomenon suggests that an initiated slip in the carbonaceous shear zone may generate potential electrical anomaly signals that can be detected by electromagnetic stations. The electrical anomaly due to Gr interconnection may be limited to anhydrous fault environments. Further experimental investigations for fluid-bearing specimens at high temperature and high pressure, applying the frequency sweep method, are required to constrain mechanical and electrical conduction mechanisms of shear zones.

Acknowledgments

This work was supported by the National Natural Science Foundation of China (Grants 41904087) and the Basic Scientific Funding of Chinese National Nonprofit Institutes of the Institute of Geology, China Earthquake Administration (Grants IGCEA1821). We thank Yan Zhan and Xiangyu Sun for discussing explanations in MT surveys and Bo Zhao for analyzing grain size distribution. We also thank Prof. Y. Gueguen and an anonymous reviewer for their constructive comments, which greatly improved this manuscript.

Open Research

All the data used for this study have been made available through Mendeley Data (https://doi.org/10.17632/p4bs2tb58h.1) (Chen et al., 2023).

Figure 1. Illustration of the friction–conductivity testing system at the Institute of Geology, China Earthquake Administration (IGCEA). (a) A low- to high-velocity rotary shear apparatus, which provides a frictional environment. (b) Appearance of the 4-wire (i.e., using wires 1–4) experimental assembly amplified from (a). The two small figures in the upper right corner show a non-specimen assembly and a specimen-bearing assembly before prepressing. (c) The electrical conductivity measurement apparatus, i.e., Keithley low-level sensitive and specialty instruments. They contain three models adapted to different electrical resistance ranges of Gr-bearing specimens (the detailed settings are presented in Table 1). (d) Diagram of a Gr-bearing specimen assembly adapted to transient electrical conductivity measurement by the 2- or 4-wire setups. An arced arrow indicates the shear direction. P_n indicates constant normal stress. (e) A schematic representation of the specimen and sections chosen for microstructural analysis (see Figure 5).

Figure 2. Frictional coefficient and electrical conductivity for the Gr–Qz mixtures sheared at a normal stress of 2 MPa. (a–b) Frictional coefficient *vs* slip displacement. (c–d) Electrical conductivity *vs* slip displacement. The slip displacement is plotted on (panels a and c) logarithmic and (panels b and d) linear scales. The percentages in the legend indicate the Gr contents of the specimens in weight ratio. $D_{\sigma ch}$, $D_{\mu ss}$, and $D_{\sigma ss}$ denote the characteristic displacements at which the electrical conductivity initiates significant changes and at which the evolution of friction coefficient and electrical conductivity reach steady states, respectively (marked as yellow diamond, pentagram, and square symbols on each curve, respectively). We note that the final jump and hold-time data (v_e < 0.6 mm/s) of all experimental values were removed.

Figure 3. Frictional coefficient and electrical conductivity for the Gr–Qz mixtures sheared at a normal stress of 5 MPa**.** Details are the same as those in Figure 2.

Figure 4. Comparison of experimental data related to characteristic displacements. (a–f) Electrical conductivity and friction coefficient plotted against displacement data at displacements between $D_{\sigma ch}$ (diamond labels) and $D_{\sigma ss}$ (square labels) are highlighted by bold solid lines. Gr fractions correspond to (panels a and d) 4–10 wt.%, (panels b and e) 9–12 wt.%, and (panels c and f) 15–50 wt.%. Further details are the same as those in Figure 2. D_0 denotes the characteristic displacements at which the specimen initiates shear deformation (marked as a circle of the same color on each curve). (g–h) Variations of $D_{\sigma ch}$, $D_{\sigma ss}$, and $D_{\mu ss}$ *vs* Gr fraction in the Gr–Qz mixtures sheared under normal stresses of 2 and 5 MPa. Definitions of the symbols are the same as those in Figure 2.

Figure 5. BSE images of the Gr-bearing specimens sectioned parallel to the axis of cylindrical host blocks. (a) 0 wt.% Gr, (b) and (e) 3 wt.% Gr, (c) and (f) 9 wt.% Gr, and (d) 25 wt.% Gr, respectively. The specimen number, final slip displacement, Gr content, and normal stress of each experiment are shown above the images. Yellow dotted lines in panels b and c show boundaries of the three layers with different

degrees of shear deformation (Layers I to III with ascending shear deformation). Gr: graphite; Qz: Quartz; ER: Epoxy Resin.

Figure 6. Microphotographs of deformed and undeformed layers for specimen. It is an unepoxied piece of the gouge layer recovered after the run LHV2429 (12 wt.% Gr at 2 MPa). (a) Geometry of the specimen and location of the spot for SEM. (b–c) SE images of the upper surface of the slip-localized zone (akin to the top surface of Layer I in Figures 5b–5c). (d–f) BSE image of the weakly or undeformed zone (akin to Layer III in Figures 5b–5c).

Figure 7. Schematic diagram of the fitting μ_{ss}–X_{Gr} relationship (solid blue line), the fitted σ_{ss}–X_{Gr} relationship (solid red line), and four classes of frictional textures for Gr–Qz mixtures. The cartoon shows the proposed graphite–cortex clast (GCC) fabric.

Figure 8. Electrical conductivity *vs.* X_{Gr}. Experimental values of the initial electrical conductivity (σ_0) at 2 MPa (solid red line) and 5 MPa (solid blue line) and a fitting curve (solid black line) of the steady-state electrical conductivity (σ_{ss}) plotted against the Gr volume percentage (X_{Gr}) for the Qz–Gr mixtures. The grey dashed line shows the conductive trend of identical mixtures in this study under uniaxial compaction at 0.1–300.0 MPa (Chen et al., 2017). The orange regime (0.100–0.005 S/m) indicates the general range of highly conductive field values in shear zones derived from magnetotelluric surveys (e.g., Pous et al., 2004; Ritter et al., 2005; Wannamaker et al., 2002; Zhao et al., 2012).

Figure 9. Schematic diagram of an electromagnetic station layout across a carbonaceous fault zone. The inset indicates the variations of shear stress (τ) and electrical conductivity (σ) of the initiated slip zone.

Table 1. Summary of electrical conductivity measurement models.

Gr wt.%	R_E range	Measurement model	Accuracy
0–3%	> 200 GΩ	4-wire setup (using wires 1–4), $R_E=E/I$, where constant DC current (I) is supplied by the 6221 AC and DC Current Source and electrical potential (E) is measured by the 6514 System Electrometer.	±0.46%
4–12%	200 Ω–200 GΩ	2-wire setup (using wires 1–2), where R_E is directly measured by the 6514 System Electrometer.	±1.50%
15–100%	< 200 Ω	4-wire (using wires 1–4), $R_E=E/I$, where I is supplied by the 6221 AC and DC Current Source and E is measured by the 2182A Nanovoltmeter.	±0.42%

Table 2. Summary of the obtained experimental data.

No.	Specimen	Gr%	error	$D_{\mu ss}$	μ_{ss}	$\mu_{ss}^{(+)/(-)}$	$D_{\sigma ch}$	$D_{\sigma ss}$	σ_0	σ_{ss}	$\sigma_{ss}^{(+)}$	$\sigma_{ss}^{(-)}$
		vol.%	±vol.%	m			m	m	S/m	S/m	S/m	S/m
Series I (2 MPa)												
LHV2051	100 wt.% Qz	0.00	0.00	nd	nd	nd	nd	0.894	1.54×10^{-7}	4.38×10^{-11}	3.56×10^{-11}	1.96×10^{-11}
LHV2416	3 wt.% Gr+97 wt.% Qz	3.44	0.08	2.229	0.79	0.01	nd	2.89×10^{-4}	1.10×10^{-9}	8.68×10^{-11}	9.39×10^{-11}	4.51×10^{-11}
LHV1374	4 wt.% Gr+96 wt.% Qz	4.58	0.09	0.397	0.80	0.03	0.500	1.161	1.80×10^{-10}	1.40×10^{-3}	1.16×10^{-3}	6.34×10^{-4}
LHV1372	5 wt.% Gr+95 wt.% Qz	5.72	0.11	0.566	0.54	0.01	0.233	0.788	5.53×10^{-10}	5.90×10^{-3}	5.05×10^{-3}	2.72×10^{-3}
LHV1373	6 wt.% Gr+94 wt.% Qz	6.85	0.12	0.525	0.62	0.04	0.158	1.048	3.59×10^{-10}	0.089	0.087	0.044
LHV1371	9 wt.% Gr+91 wt.% Qz	10.23	0.16	0.508	0.78	0.00	7.01×10^{-4}	0.206	6.93×10^{-10}	0.345	0.256	0.147
LHV2052	10 wt.% Gr+90 wt.% Qz	11.35	0.17	nd	nd	nd	0.004	0.113	2.28×10^{-10}	0.018	4.36×10^{-3}	3.50×10^{-3}
LHV2429	12 wt.% Gr+88 wt.% Qz	13.57	0.20	nd	nd	nd	1.94×10^{-4}	0.004	0.268	4.367	2.267	1.492
LHV1380/2050	15 wt.% Gr+85 wt.% Qz	16.89	0.23	0.321	0.62	0.03	1.79×10^{-4}	0.009	1.679	1.473	0.060	0.058
LHV2418	25 wt.% Gr+75 wt.% Qz	27.74	0.31	0.150	0.19	0.01	3.89×10^{-4}	0.003	32.59	54.61	9.211	7.882
LHV2419	50 wt.% Gr+50 wt.% Qz	53.53	0.37	0.339	0.11	0.00	4.39×10^{-4}	0.003	171.0	421.5	31.68	29.47
Series II (5 MPa)												
LHV2057	100 wt.% Qz	0.00	0.00	nd	nd	nd	nd	0.170	8.15×10^{-8}	1.78×10^{-11}	1.13×10^{-12}	1.06×10^{-12}
LHV1823/2054	3 wt.% Gr+97 wt.% Qz	3.44	0.08	0.361	0.85	0.03	nd	0.594	2.70×10^{-10}	1.57×10^{-10}	2.00×10^{-11}	1.77×10^{-11}
LHV1375*	6 wt.% Gr+94 wt.% Qz	6.85	0.12	0.413	0.80	0.06	0.175	0.743	8.65×10^{-9}	0.011	0.023	7.29×10^{-3}
LHV2055	9 wt.% Gr+91 wt.% Qz	10.23	0.16	0.407	0.84	0.12	7.94×10^{-4}	0.057	5.64×10^{-4}	0.359	0.085	0.069
LHV2056	15 wt.% Gr+85 wt.% Qz	16.89	0.23	0.337	0.74	0.03	5.98×10^{-4}	0.010	13.57	54.37	12.00	9.828
LHV2053	100 wt.% Gr	100	0.00	0.283	0.10	0.00	0.000	0.000	1095	1077	22.19	21.74

Gr: graphite; Qz: quartz; $\mu_{ss:}$ steady-state frictional coefficient; $\mu_{ss}^{(+)/(-)}$: standard deviation of μ_{ss}; $D_{\mu ss}$: slip displacement as μ achieved μ_{ss}; σ_0: initial electrical conductivity; σ_{ss}: steady-state electrical conductivity; $\sigma_{ss}^{(+)}/\sigma_{ss}^{(-)}$: standard deviation of σ_{ss}; $D_{\sigma ch}$: slip displacement as conductivity initiated logarithmic change; $D_{\sigma ss}$: slip displacement as σ achieved σ_{ss}, and nd indicates that the parameter could not be determined due to erratic frictional behavior.

Table 3. Fitted parameters of Equation 2 for the relationships between μ_{ss} and X_{Gr}. Fitted parameters proposed by Oohashi et al. (2013) are also listed.

μ_{Qz}	μ_{Gr}	X_{cw}	S	Data source and slip rate
0.73	0.10	0.223	8.97	This study; 1 mm/s
0.65	0.09	0.128	1.82	Oohashi et al., 2013; 0.2 mm/s
0.57	0.09	0.118	1.56	Oohashi et al., 2013; 21–56 mm/s

μ_{Qz} and μ_{Gr}: μ of pure Qz and Gr, respectively; X_{cw}: critical slip-weakening fraction for X_{Gr}; S: slope parameter.

Table 4. Fitted parameters of Equation 3 for the relationships between σ_{ss} and X_{Gr}. Fitted parameters proposed by Chen et al. (2017) are also listed.

X_c vol.%	σ_{Qz} S/m	σ_{Gr} S/m	α	r	Data source and experiment conditions
11.3	2.28×10^{-10}	>171.0			Initial compaction at 2 MPa
6.8	2.70×10^{-10}	1095.0			Initial compaction at 5 MPa
3.4	1.11×10^{-10}	1077.0	1.29	3.36	Post-shear at 2–5 MPa
6.0	1.32×10^{-10}	889.6	3.37	2.53	Chen et al., 2017; uniaxial compression

α: geometric factor of the conductor (Gr); r: nondimensional parameter; X_c: threshold value of X_{Gr}; σ_{Qz}: electrical conductivity of the insulating matrix (Qz); σ_{Gr}: electrical conductivity of the conductor (Gr).

References

Boullier, A.-M., Yeh, E.-C., Boutareaud, S., Song, S.-R., & Tsai, C.-H. (2009). Microscale anatomy of the 1999 Chi-Chi earthquake fault zone. *Geochemistry, Geophysics, Geosystems*, *10*(3), Q03016. https://doi.org/10.1029/2008GC002252

Boulton, C., Yao, L., Faulkner, D. R., Townend, J., Toy, V. G., Sutherland, R., et al. (2017). High-velocity frictional properties of Alpine Fault rocks: Mechanical data, microstructural analysis, and implications for rupture propagation. *Journal of Structural Geology*, *97*, 71-92. https://doi.org/10.1016/j.jsg.2017.02.003

Boutareaud, S., Boullier, A.-M., Andréani, M., Calugaru, D.-G., Beck, P., Song, S.-R., et al. (2010). Clay clast aggregates in gouges: New textural evidence for seismic faulting. *Journal of Geophysical Research: Solid Earth*, *115*(B2), B02408. https://doi.org/10.1029/2008JB006254

Byerlee, J. (1978). Friction of rocks. *pure and applied geophysics*, *116*(4), 615-626. https://doi.org/10.1007/bf00876528

Chen, J.-Y., Yang, X.-S., & Chen, J.-Y. (2017). Experimental studies on the relationship between carbonaceous structure and electrical conductivity of the Longmenshan fault zone. *Chinese Journal of Geophysics (in Chinese)*, *60*(9), 3475-3492. https://doi.org/10.6038/cjg20170917

Chen, J. (2022). The Effect of Quartz Particle Size on the Frictional and Electrically Conductive Properties of Mixed Graphite–Quartz Gouges. *Frontiers in Earth Science*, *10*, 913315. https://doi.org/10.3389/feart.2022.913315

Chen, J., Chen, J., Yao, L., & Ma, X. (2023). Analytical data and mechanical-electrical data of synthetic Qz-Gr mixtures (Version 1) [Dataset]. Mendeley Data. https://doi.org/10.17632/p4bs2tb58h.1

Chen, J., Gaillard, F., Villaros, A., Yang, X., Laumonier, M., Jolivet, L., et al. (2018). Melting conditions in the modern Tibetan crust since the Miocene. *Nature communications*, *9*(1), 3515. https://doi.org/10.1038/s41467-018-05934-7

Chen, J., Yang, X., Ma, S., Yang, T., & Niemeijer, A. (2016). Hydraulic properties of samples retrieved from the Wenchuan earthquake Fault Scientific Drilling Project Hole-1 (WFSD-1) and the surface rupture zone: Implications for coseismic slip weakening and fault healing. *Geochemistry, Geophysics, Geosystems*, *17*(7), 2717-2744. https://doi.org/10.1002/2016GC006376

Collettini, C., Niemeijer, A., Viti, C., & Marone, C. (2009). Fault zone fabric and fault weakness. *Nature*, *462*, 907. https://doi.org/10.1038/nature08585

Collettini, C., Tesei, T., Scuderi, M. M., Carpenter, B. M., & Viti, C. (2019). Beyond Byerlee friction, weak faults and implications for slip behavior. *Earth and Planetary Science Letters*, *519*, 245-263. https://doi.org/10.1016/j.epsl.2019.05.011

Crawford, B. R., Faulkner, D. R., & Rutter, E. H. (2008). Strength, porosity, and permeability development during hydrostatic and shear loading of synthetic quartz-clay fault gouge. *Journal of Geophysical Research: Solid Earth*, *113*, B03207. https://doi.org/10.1029/2006JB004634

Dieterich, J. H. (1992). Earthquake nucleation on faults with rate-and state-dependent strength. *Tectonophysics*, *211*(1), 115-134. https://doi.org/https://doi.org/10.1016/0040-1951(92)90055-B

Du, X. (2011). Two types of changes in apparent resistivity in earthquake prediction. *Science China Earth Sciences*, *54*(1), 145-156. https://doi.org/10.1007/s11430-010-4031-y

Duba, A. G., & Shankland, T. J. (1982). Free carbon & electrical conductivity in the Earth's mantle. *Geophysical Research Letters*, *9*(11), 1271-1274. https://doi.org/10.1029/GL009i011p01271

Frost, B. R., Fyfe, W. S., Tazaki, K., & Chan, T. (1989). Grain-boundary graphite in rocks and implications for high electrical conductivity in the lower crust. *Nature*, *340*(6229), 134-136.

https://doi.org/10.1038/340134a0

Glover, P. W. J., & Ádám, A. (2008). Correlation between crustal high conductivity zones and seismic activity and the role of carbon during shear deformation. *Journal of Geophysical Research: Solid Earth*, *113*(B12), B12210. https://doi.org/10.1029/2008JB005804

Glover, P. W. J., & Vine, F. J. (1992). Electrical conductivity of carbon-bearing granulite at raised temperatures and pressures. *Nature*, *360*(6406), 723-726. https://doi.org/10.1038/360723a0

Gueguen, Y., & Dienes, J. (1989). Transport properties of rocks from statistics and percolation. *Mathematical Geology*, *21*(1), 1-13. https://doi.org/10.1007/BF00897237

Guo, H., & Keppler, H. (2019). Electrical Conductivity of NaCl-Bearing Aqueous Fluids to 900 °C and 5 GPa. *Journal of Geophysical Research: Solid Earth*. https://doi.org/doi:10.1029/2018JB016658

Haak, V., Simpson, F., Bahr, K., Bigalke, J., Eisel, M., Harms, U., et al. (1997). KTB and the electrical conductivity of the crust. *Journal of Geophysical Research*, *102*(B8), 18289-18306. https://doi.org/10.1029/96JB03861

Han, M., Yang, X., Yao, L., Chen, J., & Ma, S. (2019). A research on the conductivity characteristics of carbon-rich fault zones based on the middle-to high-velocity frictional experiments. *Chinese Journal of Geophysics (in Chinese)*, *63*(3), 967-981. https://doi.org/10.6038/cjg2019M0143

Han, R., & Hirose, T. (2012). Clay–clast aggregates in fault gouge: An unequivocal indicator of seismic faulting at shallow depths? *Journal of Structural Geology*, *43*, 92-99. https://doi.org/10.1016/j.jsg.2012.07.008

Hickman, S., Sibson, R., & Bruhn, R. (1995). Introduction to special section: Mechanical involvement of fluids in faulting. *Journal of Geophysical Research: Solid Earth (1978–2012)*, *100*(B7), 12831-12840. https://doi.org/10.1029/95JB01121

Hirono, T., Ujiie, K., Ishikawa, T., Mishima, T., Hamada, Y., Tanimizu, M., et al. (2009). Estimation of temperature rise in a shallow slip zone of the megasplay fault in the Nankai Trough. *Tectonophysics*, *478*(3-4), 215-220. https://doi.org/10.1016/j.tecto.2009.08.001

Honkura, Y., Oshiman, N., Matsushima, M., Barış, Ş., Kemal Tunçer, M., Bülent Tank, S., et al. (2013). Rapid changes in the electrical state of the 1999 Izmit earthquake rupture zone. *Nature communications*, *4*(1), 2116. https://doi.org/10.1038/ncomms3116

Hou, L., Ma, S., Shimamoto, T., Chen, J., Yao, L., Yang, X., et al. (2012). Internal structures and high-velocity frictional properties of a bedding-parallel carbonate fault at Xiaojiaqiao outcrop activated by the 2008 Wenchuan earthquake. *Earthquake Science*, *25*(3), 197-217. https://doi.org/10.1007/s11589-012-0846-2

Hou, M., He, Y., Jang, B. G., Sun, S., Zhuang, Y., Deng, L., et al. (2021). Superionic iron oxide–hydroxide in Earth's deep mantle. *Nature Geoscience*, *14*(3), 174-178. https://doi.org/10.1038/s41561-021-00696-2

Huang, Q. (2002). One possible generation mechanism of co-seismic electric signals. *Proceedings of the Japan Academy, Series B*, *78*(7), 173-178. https://doi.org/10.2183/pjab.78.173

Kedar, L., Bond, C. E., & Muirhead, D. (2020). Carbon ordering in an aseismic shear zone: Implications for Raman geothermometry and strain tracking. *Earth and Planetary Science Letters*, *549*, 116536. https://doi.org/10.1016/j.epsl.2020.116536

Kim, J. H., Ree, J.-H., Hirose, T., & Oohashi, K. (2022). Formation of clast-cortex aggregates in experimental fault gouges. *Tectonophysics*, *839*, 229524. https://doi.org/10.1016/j.tecto.2022.229524

Kirilova, M., Toy, V., Rooney, J. S., Giorgetti, C., Gordon, K. C., Collettini, C., et al. (2018a).

Structural disorder of graphite and implications for graphite thermometry. *Solid Earth*, *9*(1), 223-231. https://doi.org/10.5194/se-9-223-2018

Kirilova, M., Toy, V. G., Timms, N., Halfpenny, A., Menzies, C., Craw, D., et al. (2018b). Textural changes of graphitic carbon by tectonic and hydrothermal processes in an active plate boundary fault zone, Alpine Fault, New Zealand. *Geological Society, London, Special Publications*, *453*(1), 205-223. https://doi.org/10.1144/SP453.13

Kouketsu, Y., Shimizu, I., Wang, Y., Yao, L., Ma, S., & Shimamoto, T. (2017). Raman spectra of carbonaceous materials in a fault zone in the Longmenshan thrust belt, China; comparisons with those of sedimentary and metamorphic rocks. *Tectonophysics*, *699*, 129-145. https://doi.org/10.1016/j.tecto.2017.01.015

Kuo, L.-W., Sone, H., Luzin, V., Yeh, E.-C., Hsu, Y.-J., & Tan, E. (2022). Gouge fabrics reset by thermal pressurization record stress on faults after earthquakes. *Geology*, *50*, 1033-1037. https://doi.org/10.1130/g50217.1

Kuo, L. W., Li, H. B., Smith, S. A. F., Di Toro, G., Suppe, J., Song, S. R., et al. (2014). Gouge graphitization and dynamic fault weakening during the 2008 Mw 7.9 Wenchuan earthquake. *Geology*, *42*(1), 47-50. https://doi.org/10.1130/g34862.1

Logan, J. M., Dengo, C. A., Higgs, N. G., & Wang, Z. Z. (1992), Chapter 2 Fabrics of Experimental Fault Zones: Their Development and Relationship to Mechanical Behavior. in *International Geophysics*, edited by B. Evans and T.-f. Wong, pp. 33-67, Academic Press, doi:10.1016/S0074-6142(08)62814-4

Lu, J., Xie, T., Li, M., Wang, Y., Ren, Y., Gao, S., et al. (2016). Monitoring shallow resistivity changes prior to the 12 May 2008 M 8.0 Wenchuan earthquake on the Longmen Shan tectonic zone, China. *Tectonophysics*, *675*, 244-257. https://doi.org/10.1016/j.tecto.2016.03.006

Lyu, M., Cao, S., Neubauer, F., Li, J., & Cheng, X. (2020). Deformation fabrics and strain localization mechanisms in graphitic carbon-bearing rocks from the Ailaoshan-Red River strike-slip fault zone. *Journal of Structural Geology*, *140*, 104150. https://doi.org/10.1016/j.jsg.2020.104150

Ma, S., Shimamoto, T., Yao, L., Togo, T., & Kitajima, H. (2014). A rotary-shear low to high-velocity friction apparatus in Beijing to study rock friction at plate to seismic slip rates. *Earthquake Science*, *27*(5), 469-497. https://doi.org/10.1007/s11589-014-0097-5

Madden, T. R., LaTorraca, G. A., & Park, S. K. (1993). Electrical conductivity variations around the Palmdale Section of the San Andreas Fault Zone. *Journal of Geophysical Research*, *98*(B1), 795-808. https://doi.org/10.1029/92jb00568

Manatschal, G. (1999). Fluid-and reaction-assisted low-angle normal faulting: evidence from rift-related brittle fault rocks in the Alps (Err Nappe, eastern Switzerland). *Journal of Structural Geology*, *21*(7), 777-793. https://doi.org/10.1016/S0191-8141(99)00069-3

Mareschal, M., Fyfe, W. S., Percival, J., & Chan, T. (1992). Grain-boundary graphite in Kapuskasing gneisses and implications for lower-crustal conductivity. *Nature*, *357*, 674-676. https://doi.org/10.1038/357674a0

Mathez, E. A., Roberts, J. J., Duba, A. G., Kronenberg, A. K., & Karner, S. L. (2008). Carbon deposition during brittle rock deformation: Changes in electrical properties of fault zones and potential geoelectric phenomena during earthquakes. *Journal of Geophysical Research: Solid Earth*, *113*(B12), B12201. https://doi.org/10.1029/2008jb005798

Monteiro Santos, F. A., Mateus, A., Almeida, E. P., Pous, J., & Mendes-Victor, L. s. A. (2002). Are some of the deep crustal conductive features found in SW Iberia caused by graphite? *Earth and*

Planetary Science Letters, *201*(2), 353-367. https://doi.org/10.1016/S0012-821X(02)00721-5

Moore, D. E., & Lockner, D. A. (2004). Crystallographic controls on the frictional behavior of dry and water-saturated sheet structure minerals. *Journal of Geophysical Research: Solid Earth*, *109*(B3), B03401. https://doi.org/10.1029/2003JB002582

Moore, D. E., & Lockner, D. A. (2011). Frictional strengths of talc‐serpentine and talc‐quartz mixtures. *Journal of Geophysical Research: Solid Earth*, *116*, B01403. https://doi.org/10.1029/2010JB007881

Nakamura, Y., Oohashi, K., Toyoshima, T., Satish-Kumar, M., & Akai, J. (2015). Strain-induced amorphization of graphite in fault zones of the Hidaka metamorphic belt, Hokkaido, Japan. *Journal of Structural Geology*, *72*, 142-161. https://doi.org/10.1016/j.jsg.2014.10.012

Nover, G., Heikamp, S., Meurer, H. J., & Freund, D. (1998). In-Situ Electrical Conductivity and Permeability of Mid-Crustal Rocks from the Ktb Drilling: Consequences for High Conductive Layers in the Earth Crust. *Surveys in Geophysics*, *19*(1), 73-85. https://doi.org/10.1023/A:1006592016176

Nover, G., Stoll, J. B., & von der Gönna, J. (2005). Promotion of graphite formation by tectonic stress - a laboratory experiment. *Geophysical Journal International*, *160*(3), 1059-1067. https://doi.org/10.1111/j.1365-246X.2005.02395.x

Oohashi, K., Hirose, T., Kobayashi, K., & Shimamoto, T. (2012). The occurrence of graphite-bearing fault rocks in the Atotsugawa fault system, Japan: Origins and implications for fault creep. *Journal of Structural Geology*, *38*, 39-50. https://doi.org/10.1016/j.jsg.2011.10.011

Oohashi, K., Hirose, T., & Shimamoto, T. (2011). Shear-induced graphitization of carbonaceous materials during seismic fault motion: Experiments and possible implications for fault mechanics. *Journal of Structural Geology*, *33*(6), 1122-1134. https://doi.org/10.1016/j.jsg.2011.01.007

Oohashi, K., Hirose, T., & Shimamoto, T. (2013). Graphite as a lubricating agent in fault zones: An insight from low- to high-velocity friction experiments on a mixed graphite-quartz gouge. *Journal of Geophysical Research: Solid Earth*, *118*, 1-18. https://doi.org/10.1002/jgrb.50175

Park, S. K., Johnston, M. J. S., Madden, T. R., Morgan, F. D., & Morrison, H. F. (1993). Electromagnetic precursors to earthquakes in the Ulf band: A review of observations and mechanisms. *Reviews of Geophysics*, *31*(2), 117-132. https://doi.org/10.1029/93RG00820

Pous, J., Muñoz, G., Heise, W., Melgarejo, J. C., & Quesada, C. (2004). Electromagnetic imaging of Variscan crustal structures in SW Iberia: the role of interconnected graphite. *Earth and Planetary Science Letters*, *217*(3), 435-450. https://doi.org/10.1016/S0012-821X(03)00612-5

Puelles, P., Ábalos, B., & Fernández-Armas, S. (2014). Graphite and quartz petrofabrics: Examples from the Ediacaran black quartzites of the Ossa-Morena Zone (SW Iberia). *Tectonophysics*, *615-616*, 53-68. https://doi.org/10.1016/j.tecto.2013.12.018

Rawat, R., & Sharma, R. (2011). Features and characterization of graphite in Almora Crystallines and their implication for the graphite formation in Lesser Himalaya, India. *Journal of Asian Earth Sciences*, *42*(1), 51-64. https://doi.org/10.1016/j.jseaes.2011.03.015

Rempe, M., Smith, S. A. F., Ferri, F., Mitchell, T. M., & Di Toro, G. (2014). Clast-cortex aggregates in experimental and natural calcite-bearing fault zones. *Journal of Structural Geology*, *68*, 142-157. https://doi.org/10.1016/j.jsg.2014.09.007

Ritter, O., Hoffmann-Rothe, A., Bedrosian, P. A., Weckmann, U., & Haak, V. (2005). Electrical conductivity images of active and fossil fault zones. *Geological Society, London, Special Publications*, *245*(1), 165-186. https://doi.org/10.1144/gsl.sp.2005.245.01.08

Roberts, J. J., Duba, A. G., Mathez, E. A., Shankland, T. J., & Kinzler, R. (1999). Carbon-enhanced electrical conductivity during fracture of rocks. *Journal of Geophysical Research: Solid Earth*, *104*(B1), 737-747. https://doi.org/10.1029/1998jb900032

Rubin, A. M., & Ampuero, J. P. (2005). Earthquake nucleation on (aging) rate and state faults. *Journal of Geophysical Research: Solid Earth*, *110*(B11). https://doi.org/10.1029/2005jb003686

Rutter, E. H., Hackston, A. J., Yeatman, E., Brodie, K. H., Mecklenburgh, J., & May, S. E. (2013). Reduction of friction on geological faults by weak-phase smearing. *Journal of Structural Geology*, *51*, 52-60. https://doi.org/10.1016/j.jsg.2013.03.008

Sawai, M., Shimamoto, T., & Togo, T. (2012). Reduction in BET surface area of Nojima fault gouge with seismic slip and its implication for the fracture energy of earthquakes. *Journal of Structural Geology*, *38*, 117-138. https://doi.org/10.1016/j.jsg.2012.01.002

Selway, K. (2013). On the causes of electrical conductivity anomalies in tectonically stable lithosphere. *Surveys in Geophysics*, *35*(1), 219-257. https://doi.org/10.1007/s10712-013-9235-1

Sinmyo, R., & Keppler, H. (2017). Electrical conductivity of NaCl-bearing aqueous fluids to 600 °C and 1 GPa. *Contributions to Mineralogy and Petrology*, *172*(1), 4. https://doi.org/10.1007/s00410-016-1323-z

Stauffer, D., & Aharony, A. (2003). *Introduction to percolation theory*, London: Taylor & Francis,

Takahashi, M., Mizoguchi, K., Kitamura, K., & Masuda, K. (2007). Effects of clay content on the frictional strength and fluid transport property of faults. *Journal of Geophysical Research: Solid Earth*, *112*(B8), B08206. https://doi.org/10.1029/2006JB004678

Tembe, S., Lockner, D. A., & Wong, T.-F. (2010). Effect of clay content and mineralogy on frictional sliding behavior of simulated gouges: Binary and ternary mixtures of quartz, illite, and montmorillonite. *Journal of Geophysical Research*, *115*, B03416. https://doi.org/10.1029/2009JB006383

Togo, T., Shimamoto, T., Ma, S., Wen, X., & He, H. (2011). Internal structure of Longmenshan fault zone at Hongkou outcrop, Sichuan, China, that caused the 2008 Wenchuan earthquake. *Earthquake Science*, *24*(3), 249-265. https://doi.org/10.1007/s11589-011-0789-z

Ujiie, K., & Tsutsumi, A. (2010). High-velocity frictional properties of clay-rich fault gouge in a megasplay fault zone, Nankai subduction zone. *Geophysical Research Letters*, *37*(24), L24310. https://doi.org/10.1029/2010gl046002

Wang, D., Karato, S.-i., & Jiang, Z. (2013). An experimental study of the influence of graphite on the electrical conductivity of olivine aggregates. *Geophysical Research Letters*, *40*(10), 2028-2032. https://doi.org/10.1002/grl.50471

Wang, Y., Ma, S., Shimamoto, T., Yao, L., Chen, J., Yang, X., et al. (2014). Internal structures and high-velocity frictional properties of Longmenshan fault zone at Shenxigou activated during the 2008 Wenchuan earthquake. *Earthquake Science*, *27*(5), 499-528. https://doi.org/10.1007/s11589-014-0096-6

Wannamaker, P. E., Jiracek, G. R., Stodt, J. A., Caldwell, T. G., Gonzalez, V. M., McKnight, J. D., et al. (2002). Fluid generation and pathways beneath an active compressional orogen, the New Zealand Southern Alps, inferred from magnetotelluric data. *Journal of Geophysical Researc: Solid Earth*, *107*(B6), ETG 6-1-ETG 6-20. https://doi.org/10.1029/2001JB000186

Watson, H. C., Roberts, J. J., & Tyburczy, J. A. (2010). Effect of conductive impurities on electrical conductivity in polycrystalline olivine. *Geophysical Research Letters*, *37*(2), L02302. https://doi.org/10.1029/2009gl041566

Yamashita, F., Fukuyama, E., & Mizoguchi, K. (2014). Probing the slip-weakening mechanism of earthquakes with electrical conductivity: Rapid transition from asperity contact to gouge comminution. *Geophysical Research Letters*, *41*(2), 341-347. https://doi.org/10.1002/2013gl058671

Yao, L., Ma, S., Shimamoto, T., & Togo, T. (2013a). Structures and high-velocity frictional properties of the Pingxi fault zone in the Longmenshan fault system, Sichuan, China, activated during the 2008 Wenchuan earthquake. *Tectonophysics*, *599*, 135-156. https://doi.org/10.1016/j.tecto.2013.04.011

Yao, L., Shimamoto, T., Ma, S., Han, R., & Mizoguchi, K. (2013b). Rapid post-seismic strength recovery of Pingxi fault gouge from the Longmenshan fault system: Experiments and implications for the mechanisms of high-velocity weakening of faults. *Journal of Geophysical Research: Solid Earth*, *118*, 1-17. https://doi.org/10.1002/jgrb.50308

Yoshida, S., Uyeshima, M., & Nakatani, M. (1997). Electric potential changes associated with slip failure of granite: Preseismic and coseismic signals. *Journal of Geophysical Research: Solid Earth*, *102*(B7), 14883-14897. https://doi.org/10.1029/97JB00729

Yu, N., Unsworth, M., Wang, X., Li, D., Wang, E., Li, R., et al. (2020). New Insights Into Crustal and Mantle Flow Beneath the Red River Fault Zone and Adjacent Areas on the Southern Margin of the Tibetan Plateau Revealed by a 3-D Magnetotelluric Study. *Journal of Geophysical Research: Solid Earth*, *125*(10), e2020JB019396. https://doi.org/10.1029/2020jb019396

Zhao, G., Unsworth, M. J., Zhan, Y., Wang, L., Chen, X., Jones, A. G., et al. (2012). Crustal structure and rheology of the Longmenshan and Wenchuan Mw 7.9 earthquake epicentral area from magnetotelluric data. *Geology*, *40*(12), 1139-1142. https://doi.org/10.1130/g33703.1

Zhao, Y., & Qian, F. (1994). Geoelectric precursors to strong earthquakes in China. *Tectonophysics*, *233*(1), 99-113. https://doi.org/10.1016/0040-1951(94)90223-2

Zhuang, Y., Su, X., Salke, N. P., Cui, Z., Hu, Q., Zhang, D., et al. (2021). The effect of nitrogen on the compressibility and conductivity of iron at high pressure. *Geoscience Frontiers*, *12*(2), 983-989. https://doi.org/https://doi.org/10.1016/j.gsf.2020.04.012

Zulauf, G., Palm, S., Petschick, R., & Spies, O. (1999). Element mobility and volumetric strain in brittle and brittle–viscous shear zones of the superdeep well KTB (Germany). *Chemical geology*, *156*(1-4), 135-149. https://doi.org/10.1016/S0009-2541(98)00189-2

Figure 1.

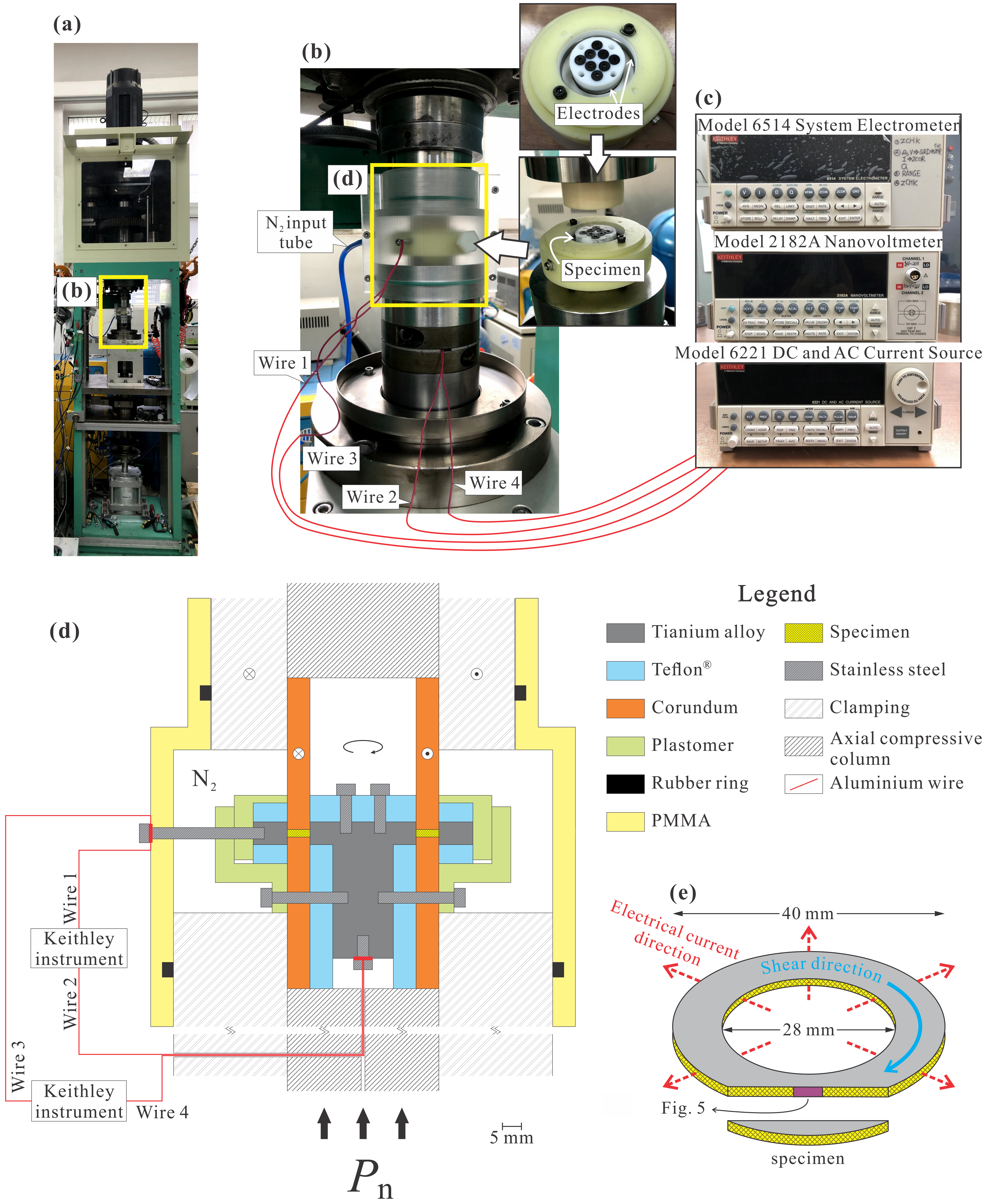

(a)
(b)
(b)
(d)
N2 input tube
Wire 1
Wire 3
Wire 2
Wire 4
Electrodes
Specimen
(c)
Model 6514 System Electrometer
Model 2182A Nanovoltmeter
Model 6221 DC and AC Current Source
(d)
N2
Wire 1
Keithley instrument
Wire 2
Wire 3
Keithley instrument
Wire 4
5 mm
Pn
Legend
Tianium alloy
Teflon®
Corundum
Plastomer
Rubber ring
PMMA
Specimen
Stainless steel
Clamping
Axial compressive column
Aluminium wire
(e)
Electrical current direction
40 mm
Shear direction
28 mm
Fig. 5
specimen

Figure 2.

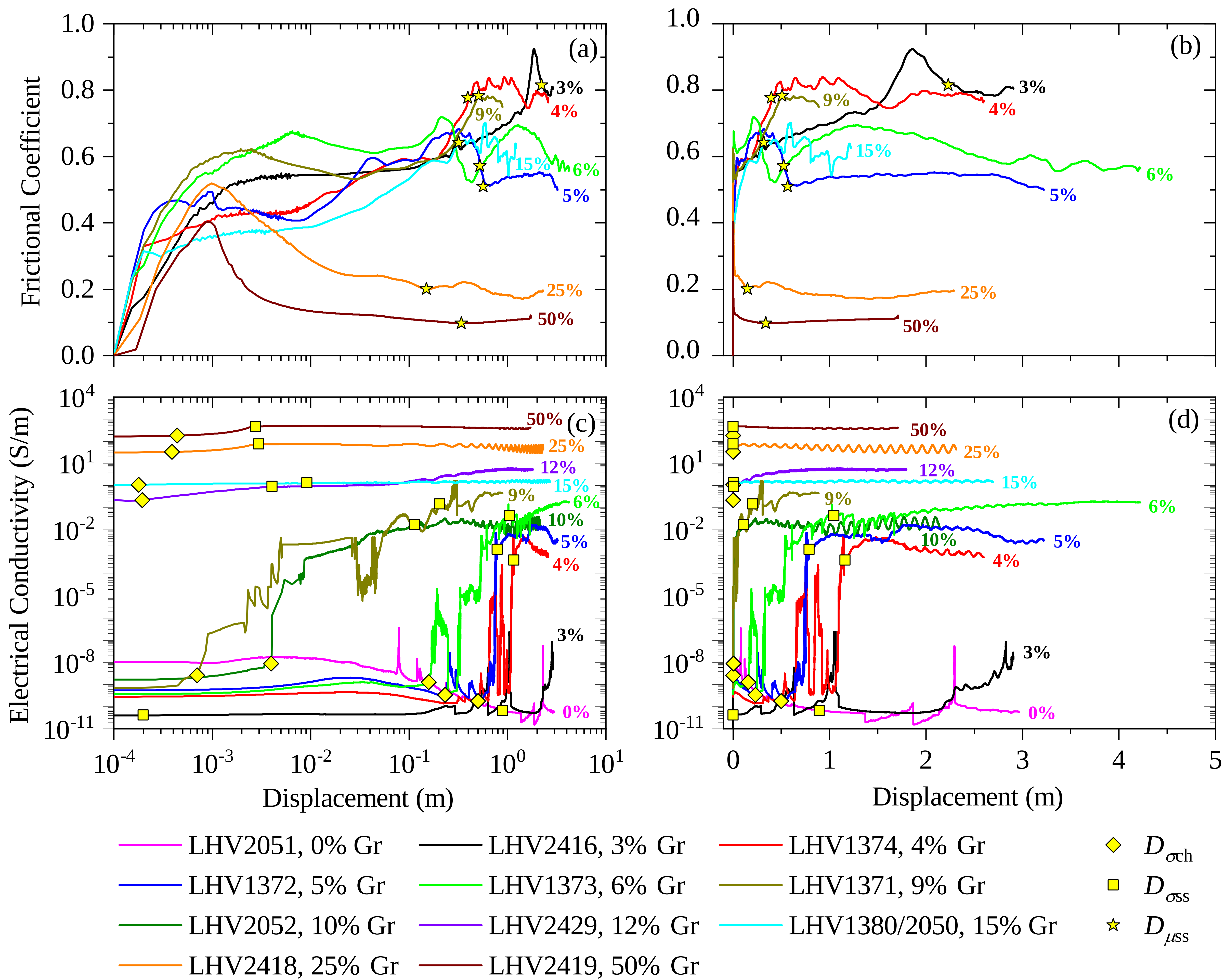

(a)
(b)
(c)
(d)
Frictional Coefficient
Electrical Conductivity (S/m)
Displacement (m)
3%
4%
5%
6%
9%
15%
25%
50%
0%
10%
12%
LHV2051, 0% Gr
LHV2416, 3% Gr
LHV1374, 4% Gr
LHV1372, 5% Gr
LHV1373, 6% Gr
LHV1371, 9% Gr
LHV2052, 10% Gr
LHV2429, 12% Gr
LHV1380/2050, 15% Gr
LHV2418, 25% Gr
LHV2419, 50% Gr
$D_{\sigma ch}$
$D_{\sigma ss}$
$D_{\mu ss}$

Figure 3.

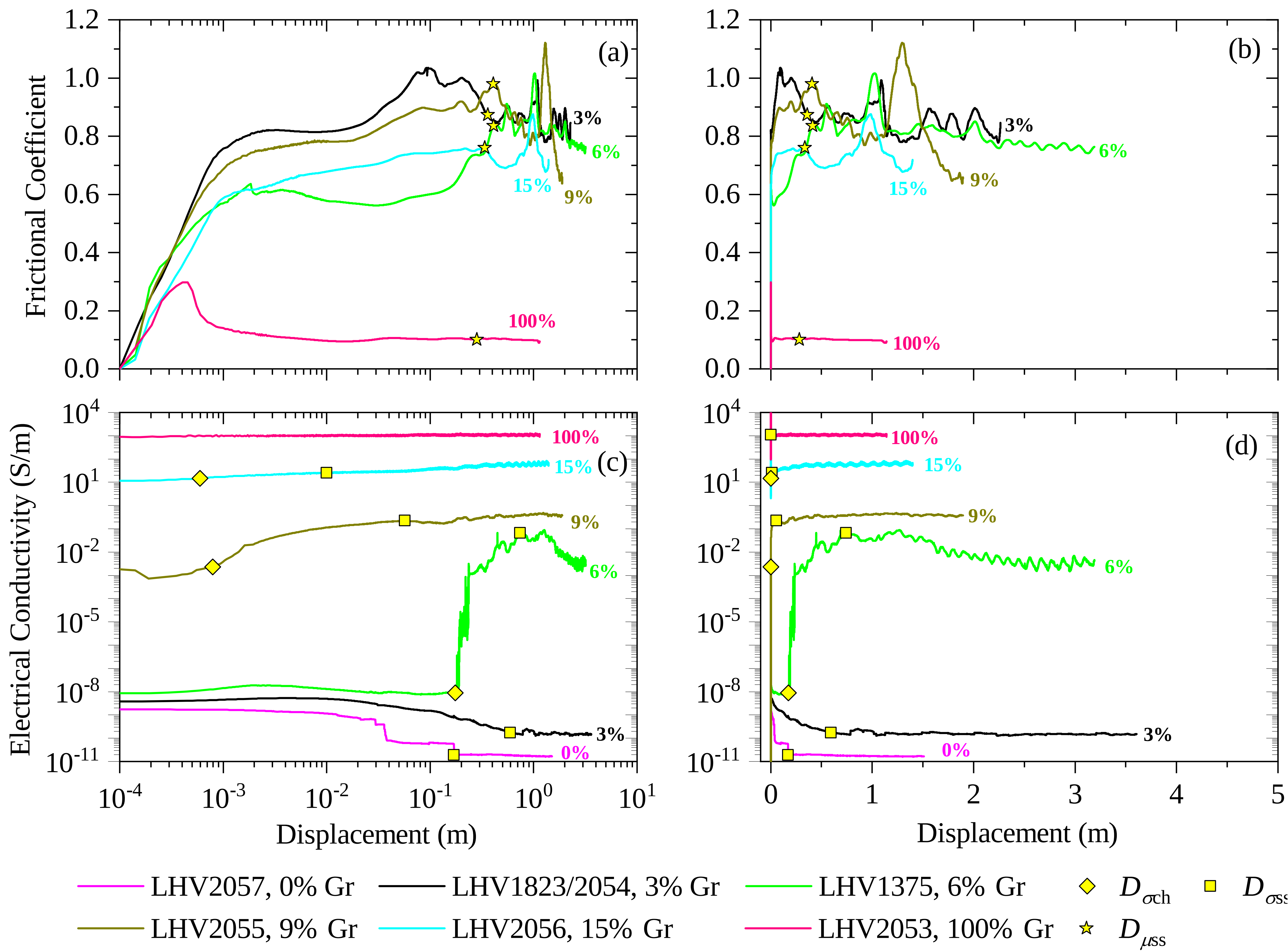

(a)
(b)
(c)
(d)
Frictional Coefficient
Electrical Conductivity (S/m)
Displacement (m)
3%
6%
9%
15%
100%
0%
LHV2057, 0% Gr
LHV1823/2054, 3% Gr
LHV1375, 6% Gr
LHV2055, 9% Gr
LHV2056, 15% Gr
LHV2053, 100% Gr
$D_{\sigma ch}$
$D_{\sigma ss}$
$D_{\mu ss}$

Figure 4.

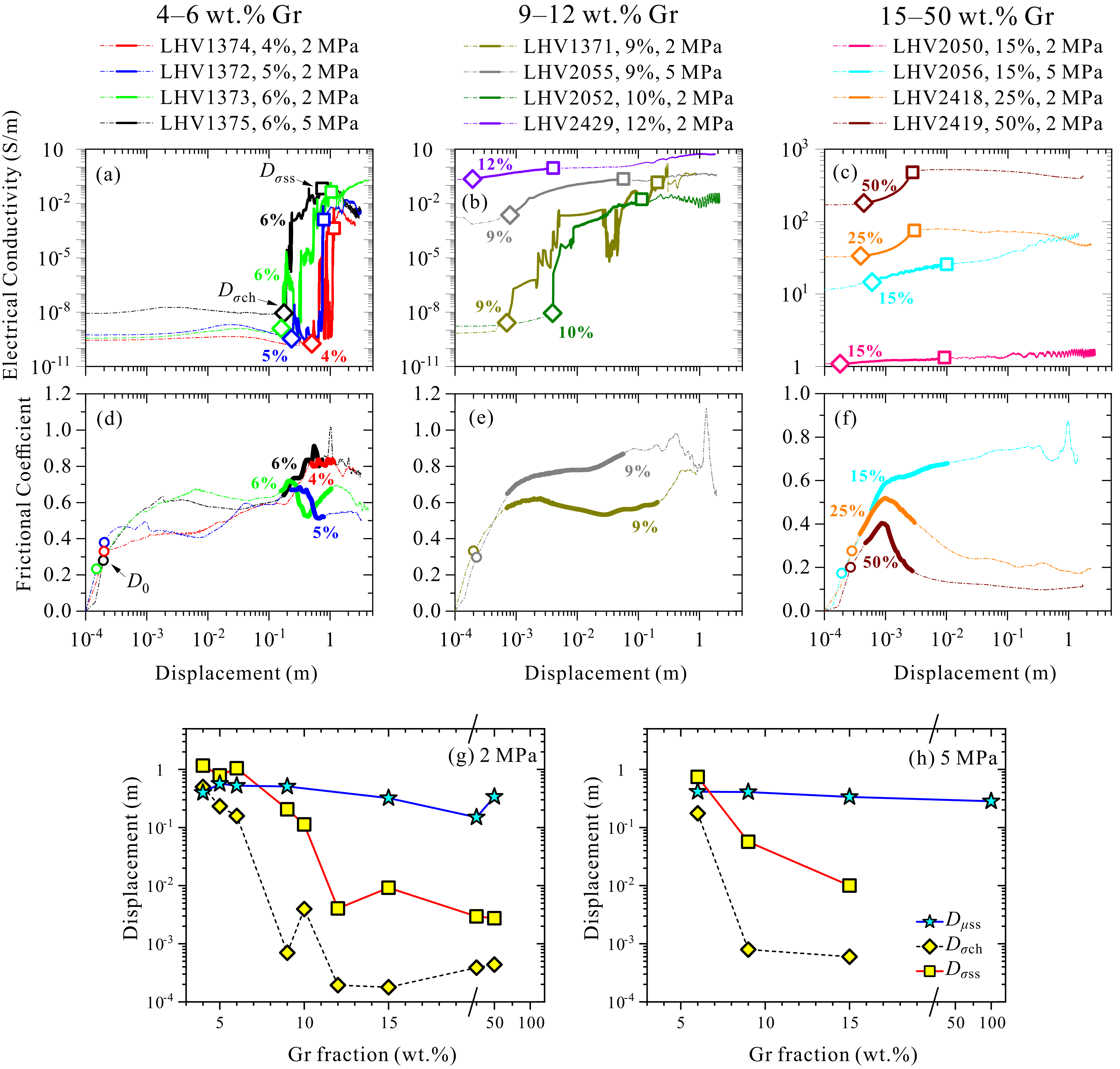

4–6 wt.% Gr
LHV1374, 4%, 2 MPa
LHV1372, 5%, 2 MPa
LHV1373, 6%, 2 MPa
LHV1375, 6%, 5 MPa
9–12 wt.% Gr
LHV1371, 9%, 2 MPa
LHV2055, 9%, 5 MPa
LHV2052, 10%, 2 MPa
LHV2429, 12%, 2 MPa
15–50 wt.% Gr
LHV2050, 15%, 2 MPa
LHV2056, 15%, 5 MPa
LHV2418, 25%, 2 MPa
LHV2419, 50%, 2 MPa
Electrical Conductivity (S/m)
Frictional Coefficient
Displacement (m)
(a) (b) (c) (d) (e) (f)
$D_{\sigma ss}$
$D_{\sigma ch}$
D_0
(g) 2 MPa
(h) 5 MPa
Gr fraction (wt.%)
$D_{\mu ss}$
$D_{\sigma ch}$
$D_{\sigma ss}$

Figure 5.

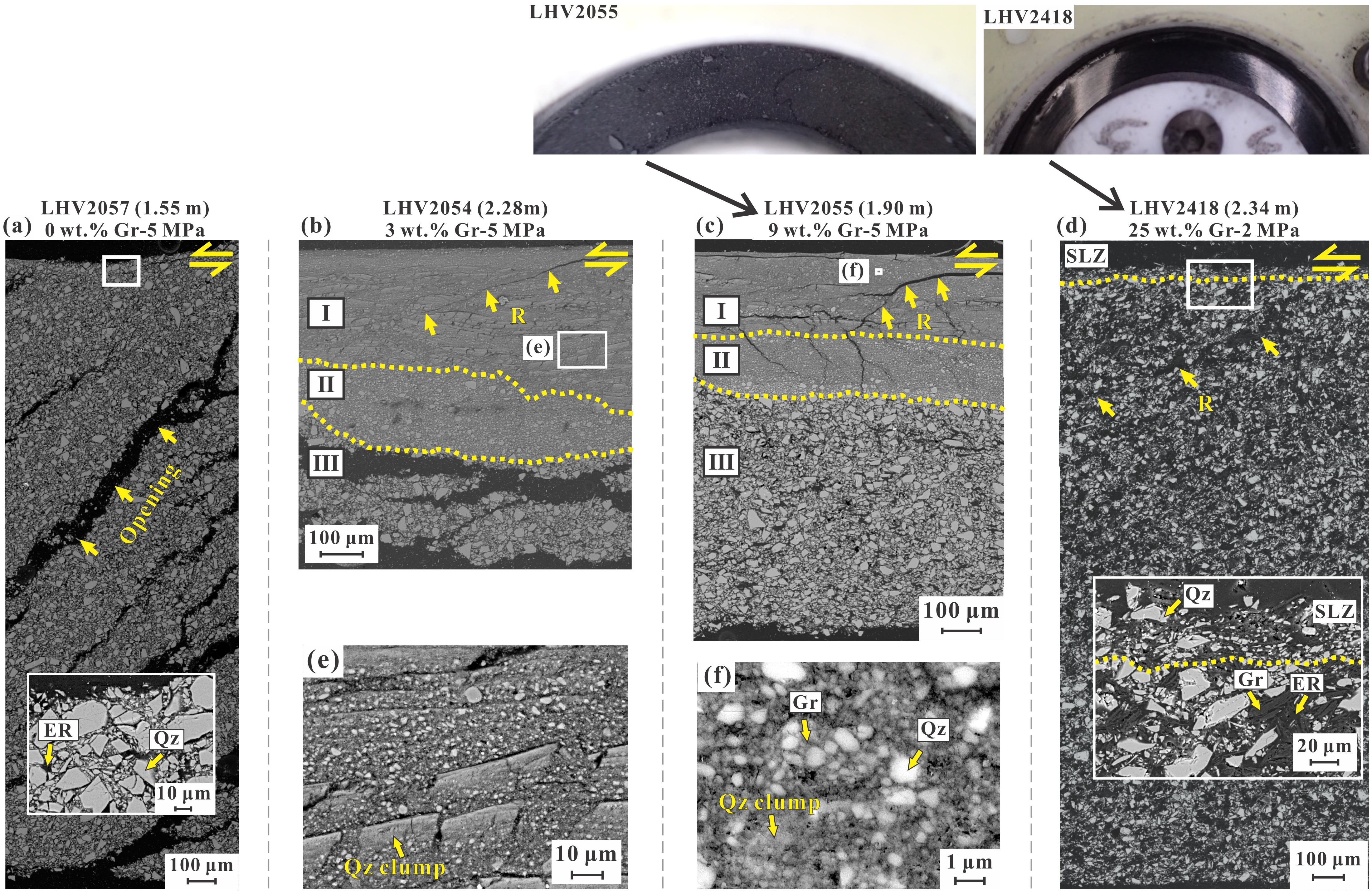

LHV2055
LHV2418
(a)
LHV2057 (1.55 m)
0 wt.% Gr-5 MPa
Opening
ER
Qz
10 µm
100 µm
(b)
LHV2054 (2.28m)
3 wt.% Gr-5 MPa
I
II
III
R
(e)
100 µm
(c)
LHV2055 (1.90 m)
9 wt.% Gr-5 MPa
(f)
I
II
III
R
100 µm
(d)
LHV2418 (2.34 m)
25 wt.% Gr-2 MPa
SLZ
R
Qz
SLZ
Gr
ER
20 µm
100 µm
(e)
Qz clump
10 µm
(f)
Gr
Qz
Qz clump
1 µm

Figure 6.

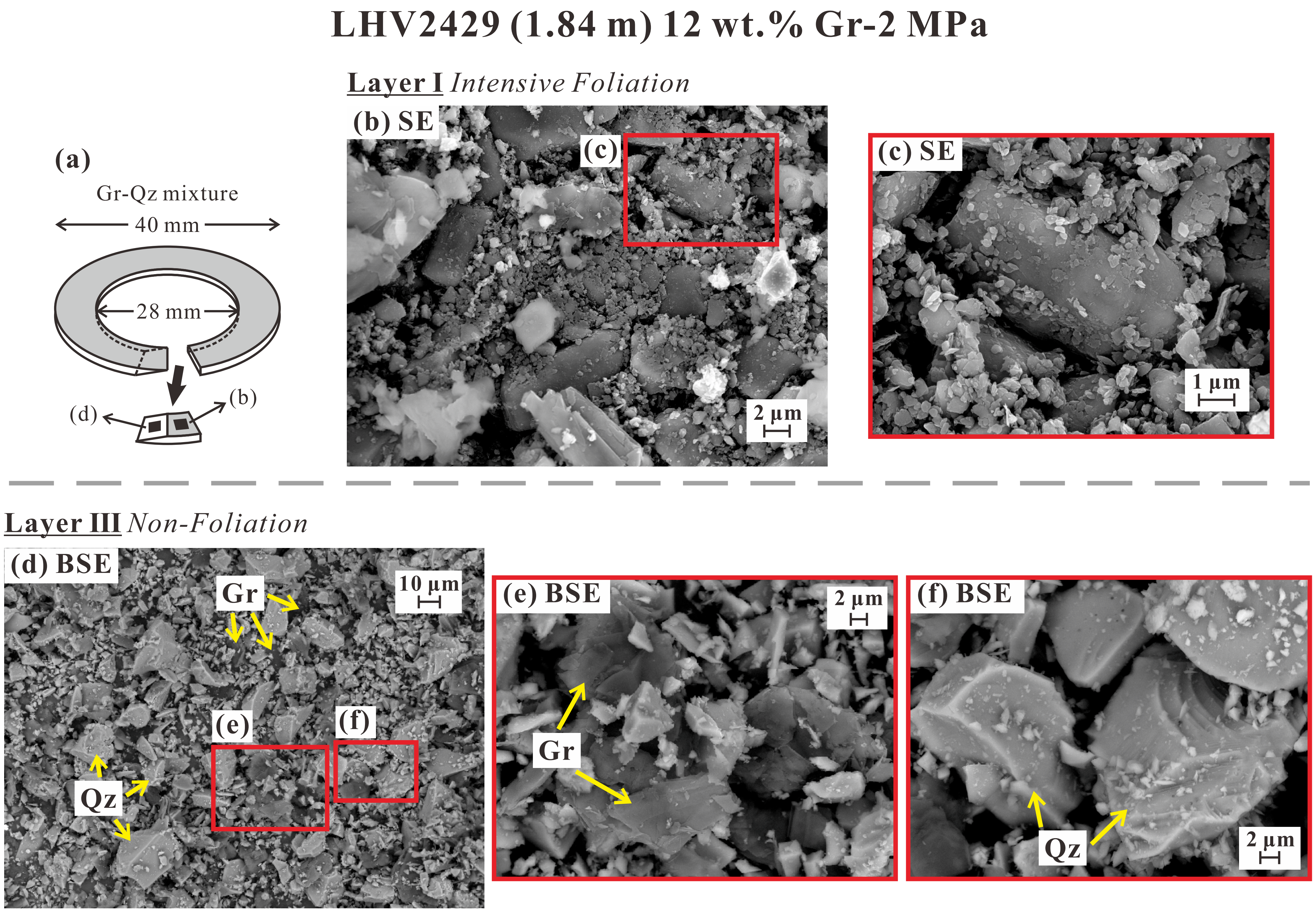
LHV2429 (1.84 m) 12 wt.% Gr-2 MPa
(a)
Gr-Qz mixture
40 mm
28 mm
(d)
(b)
Layer I Intensive Foliation
(b) SE
(c)
2 μm
(c) SE
1 μm
Layer III Non-Foliation
(d) BSE
10 μm
Gr
Qz
(e)
(f)
(e) BSE
2 μm
Gr
(f) BSE
Qz
2 μm

Figure 7.

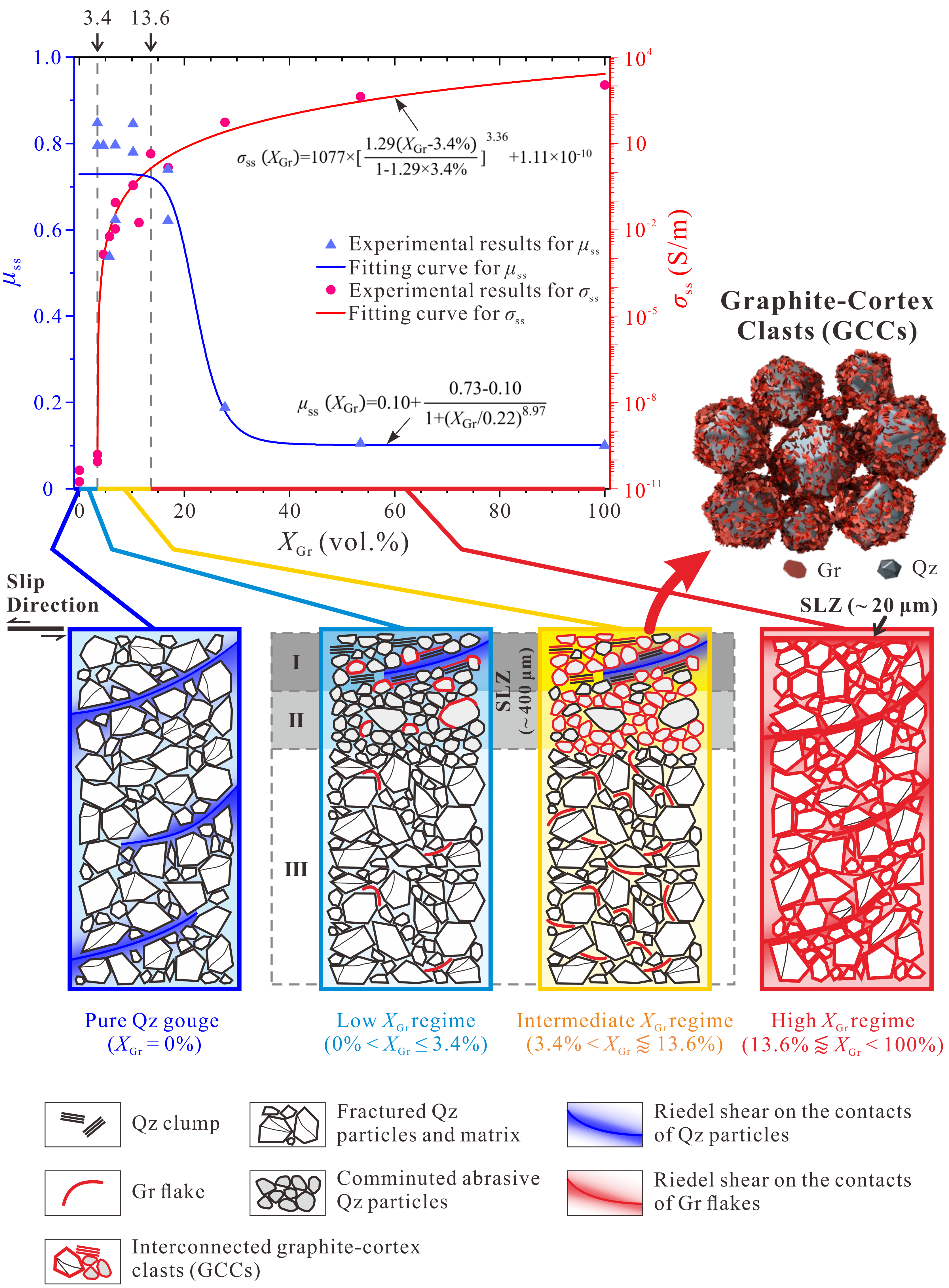

3.4
13.6
μ_{ss}
σ_{ss} (S/m)
X_{Gr} (vol.%)
$\sigma_{ss}(X_{Gr})=1077\times[\frac{1.29(X_{Gr}-3.4\%)}{1-1.29\times3.4\%}]^{3.36}+1.11\times10^{-10}$
$\mu_{ss}(X_{Gr})=0.10+\frac{0.73-0.10}{1+(X_{Gr}/0.22)^{8.97}}$
Experimental results for μ_{ss}
Fitting curve for μ_{ss}
Experimental results for σ_{ss}
Fitting curve for σ_{ss}
Graphite-Cortex Clasts (GCCs)
Gr
Qz
Slip Direction
SLZ (~ 20 µm)
SLZ (~ 400 µm)
I
II
III
Pure Qz gouge (X_{Gr} = 0%)
Low X_{Gr} regime (0% < X_{Gr} ≤ 3.4%)
Intermediate X_{Gr} regime (3.4% < X_{Gr} ≨ 13.6%)
High X_{Gr} regime (13.6% ≨ X_{Gr} < 100%)
Qz clump
Fractured Qz particles and matrix
Riedel shear on the contacts of Qz particles
Gr flake
Comminuted abrasive Qz particles
Riedel shear on the contacts of Gr flakes
Interconnected graphite-cortex clasts (GCCs)

Figure 8.

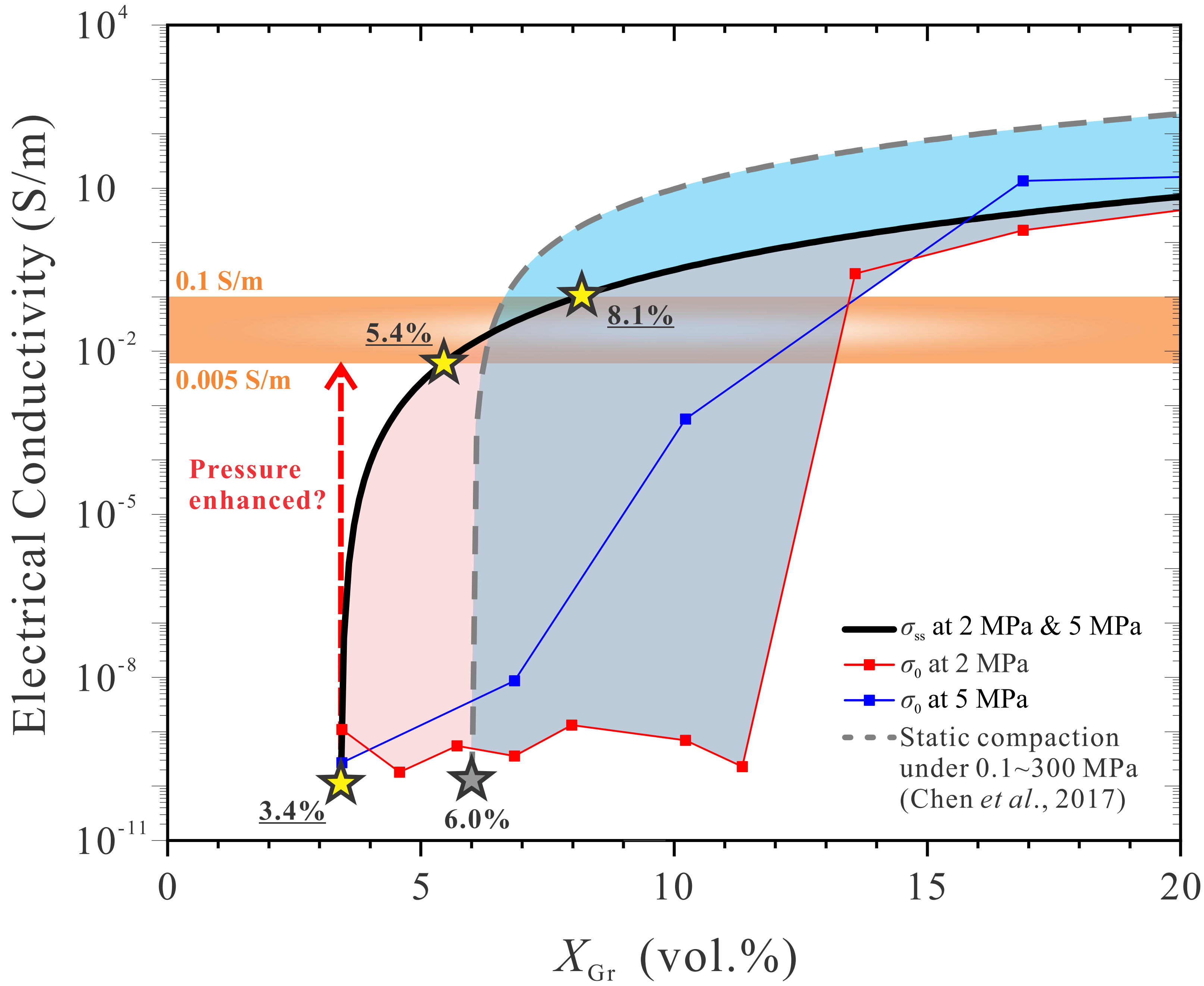

Electrical Conductivity (S/m)
10^4
10
10^-2
10^-5
10^-8
10^-11
0
5
10
15
20
X_Gr (vol.%)
0.1 S/m
0.005 S/m
5.4%
8.1%
3.4%
6.0%
Pressure enhanced?
σ_ss at 2 MPa & 5 MPa
σ_0 at 2 MPa
σ_0 at 5 MPa
Static compaction under 0.1~300 MPa (Chen et al., 2017)

Figure 9.

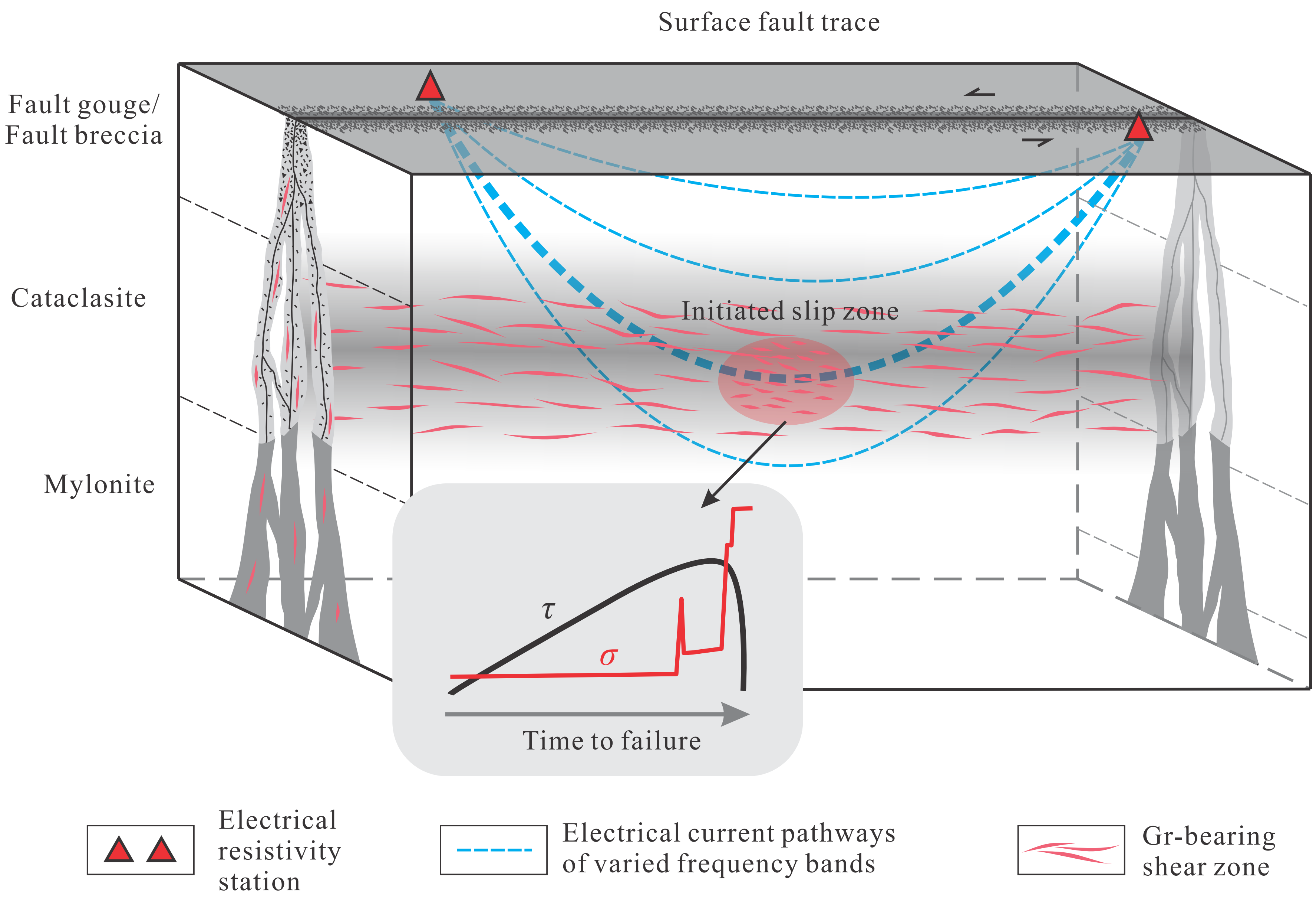
Surface fault trace
Fault gouge/
Fault breccia
Cataclasite
Mylonite
Initiated slip zone
τ
σ
Time to failure
Electrical resistivity station
Electrical current pathways of varied frequency bands
Gr-bearing shear zone